Characterization of MSS Channel Reflectance and Derived Spectral Indices for Building Consistent Landsat 1–5 Data Record

Feng Chen, Qiancong Fan, Shenlong Lou, Limin Yang, Chenxing Wang, Martin Claverie, Cheng Wang, *Senior Member, IEEE*, José Marcato Junior, *Member, IEEE*, Wesley Nunes Gonçalves, *Member, IEEE*, and Jonathan Li, *Senior Member, IEEE*

Abstract—The Landsat 1–5 multispectral scanner system (MSS) collected records of land surface mainly during 1972–1992. Investigations on MSS have been relatively limited compared with the numerous investigations on its successors, such as Thematic Mapper (TM) and Enhanced TM Plus (ETM+). The benefits of the Landsat program are not fully accomplished without the inclusion of MSS archives. Investigations on the Landsat 1–5 MSS channel reflectance characteristics wereperformed followed by derived vegetation spectral indices and the Tasseled Cap (TC) transformed features mainly using a collection of synthesized records. On average, the Landsat 4 MSS is generally comparable to the Landsat 5 MSS. The Landsat 1–3 MSSs show disagreement in channel reflectance compared with the Landsat 5 MSS, especially for the red channel (600–700 nm) and the near-infrared channel (700–800 nm). Meanwhile, the relative differences for vegetation spectral indices of the Landsat 3 MSS are mainly from -16% to -5% with the median about -11.5%, while those of the Landsat 2 MSS are mainly from -15% to -7%. Cross-validation tests and two case applications suggested that between-sensor consistency was improved generally through the transformation models generated by ordinary least-squares regression. To improve the consistency of the vegetation indices and the TC greenness, direct strategy employing respective transformation models was more effective than calculations based on the transformed channel reflectance. Considering the shortages of the Landsat MSS archives, further efforts are needed to improve its comparability with observations by other successive Landsat sensors.

Index Terms—Consistency, Landsat, multispectral scanner system (MSS), spectral response function (SRF), transformation, vegetation indices.

Feng Chen is with the Fujian Key Laboratory of Sensing and Computing for Smart Cities, School of Informatics, Xiamen University, Xiamen 361005, China, also with the Big Data Institute of Digital Natural Disaster Monitoring in Fujian, Xiamen University of Technology, Xiamen 361024, China, and also with the College of Computer and Information Engineering, Xiamen University of Technology, Xiamen 361024, China (e-mail: chenfeng105@gmail.com).

Qiancong Fan, Shenlong Lou, and Cheng Wang are with the Fujian Key Laboratory of Sensing and Computing for Smart Cities, School of Informatics, Xiamen University, Xiamen 361005, China (e-mail: fanqc@stu.xmu.edu.cn; loushenlong@stu.xmu.edu.cn; cwang@xmu.edu.cn).

Limin Yang is with the College of Resource Environment and Tourism, Capital Normal University, Beijing 10048, China (e-mail: lyang0117@yahoo.com).

Chenxing Wang is with the State Key Laboratory of Urban and Regional Ecology, Research Center for Eco-Environmental Sciences, Chinese Academy of Sciences, Beijing 100085, China (e-mail: cxwang@rcees.ac.cn).

Martin Claverie was with the Department of Geographical Sciences, University of Maryland, College Park, MD 20742 USA. He is now with the Earth and Life Institute of Université Catholique de Louvain, 1348 Louvain-la-Neuve, Belgium (e-mail: martin.claverie@uclouvain.be).

José Marcato Junior and Wesley Nunes Gonçalves are with the Faculty of Engineering, Architecture and Urbanism and Geography, Federal University of Mato Grosso do Sul, Campo Grande 79070-900, Brazil (e-mail: jose.marcato@ufms.br; wesley.goncalves@ufms.br).

Jonathan Li is with the Department of Geography and Environmental Management, University of Waterloo, Waterloo, ON N2L 3G1, Canada, and also with the Department of Systems Design Engineering, University of Waterloo, Waterloo, ON N2L 3G1, Canada (e-mail: junli@uwaterloo.ca).

Color versions of one or more of the figures in this article are available online at http://ieeexplore.ieee.org.

Digital Object Identifier 10.1109/TGRS.2020.2992609

I. INTRODUCTION

THE Landsat project, as a part of the National Land Imaging Program jointly supported by the U.S. Geological Survey (USGS) and the National Aeronautics and Space Administration (NASA), has contributed to the longest and most geographically comprehensive record of Earth observation with moderate spatial resolutions since 1972 [1], [2]. The free data policy, implemented in 2008 [3], contributed mostly to the increasing applications of the Landsat archive, especially in time-series analyses [1], [2], [4]–[6]. More than 8.13 million images up to September 30, 2018, had been available in a consistent archive acquired by all seven successive Landsat satellites (https://landsat.usgs.gov/landsat-archive) due to the contribution of the USGS Landsat Global Archive Consolidation (LGAC) initiative that began in 2010 [4]. In particular, the Landsat 1–5 multispectral scanner system (MSS) collected global records of land surface mainly during 1972–1992 with additional but limited acquisitions until January 2013 (see Table I). More than 1.32 million MSS scenes had been absorbed into the USGS Landsat archive up to September 30, 2018 (https://landsat.usgs.gov/landsat-archive), similar to the previous observation, with nearly two million scenes expected after completion of the LGAC initiative [4]. The MSS data are considered the most valuable for time-series analyses, as captured by the first Landsat missions, and,

TABLE I
GENERAL INFORMATION ABOUT THE LANDSAT 1–5 MSS SENSORS

	Landsat1	Landsat2	Landsat3	Landsat4	Landsat5
Launch	23 July 1972	22 Jan. 1975	5 Mar. 1978	16 July 1982	1 Mar. 1984
Ending	6 Jan. 1978	27 July 1983	7 Sept. 1983	14 Dec. 1993[a]	5 June 2013[b]
Channels (nm)		Green: 500-600 Red: 600-700 NIR1: 700-800 NIR2: 800-1100			
Resolution (m)		60×60[c]			
Repeat cycle (day)		18		16	
WRS[d]		WRS-1		WRS-2	

Landsat 1-3 carried two sensors including the Return Beam Vidicon and the Multispectral Scanner System (MSS). In addition to the MSS, Landsat 4 and Landsat 5 carried a new instrument called Thematic Mapper (TM). By the way, the Landsat 3 MSS had an additional channel in thermal infrared region (10.4-12.6 μm), with purposes for test until 11 July 1978.
[a]Actually, Landsat 4 was finally decommissioned 15 June 2001.
[b]Acquisitions of the Landsat 5 MSS data over the United States ceased in 1992 and the global acquisitions ended in 1999. Limited acquisitions were made from June 2012 through January 2013, after the loss of the TM sensor on the satellite.
[c]Currently, the Landsat MSS archival imagery in Collection 1 Level-1 data product available for download is provided with a spatial resolution of 60 m×60 m, although original resolution was 57 m×79 m.
[d]The Worldwide Reference System (WRS) is a global notation system for Landsat data. Landsat 1-3 had an 18-day revisit cycle on the WRS-1, whereas the successors (i.e., Landsat 4-5) had a 16-day revisit cycle on the WRS-2 (https://landsat.gsfc.nasa.gov/the-worldwide-reference-system/). All information listed was collected from https://landsat.usgs.gov/.
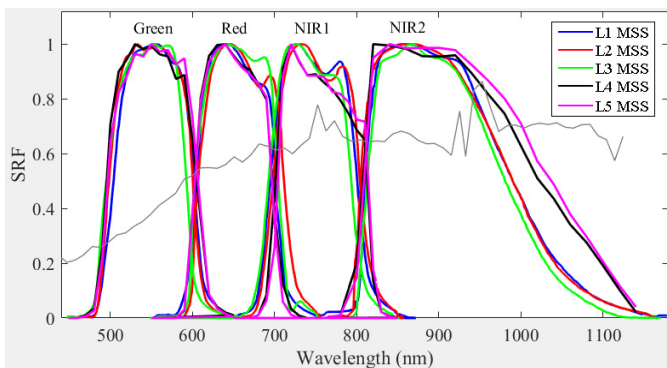

Fig. 1. Comparison of the SRFs for individual channels of the Landsat 1–5 MSS, including the channels of green (500–600 nm), red (600–700 nm), NIR1 (700–800 nm), and NIR2 (800–1100 nm). The SRFs are accessible at https://landsat.gsfc.nasa.gov/spectral-response-of-the-multispectral-scanner-system-in-band-band-average-relative-spectral-response/. The gray line shows a reflectance spectrum of forest over corresponding spectral range observed by Hyperion.

particularly, are the unique globally acquired data sources with a moderate spatial resolution for 1972–1984 [2]. The MSS, onboard Landsat 1–5, presents four spectral channels, covering visible and near-infrared (NIR) spectral regions (see Table I), whereas variations among the sensors are observable to some extent (see Fig. 1).

Although the Landsat program is considered a relatively consistent mission [2], quite small sensor differences may have a significant impact depending on data application [7]. For example, the characterization differences were shown between the Landsat 7 Enhanced Thematic Mapper (ETM+)

and the Landsat 8 Operational Land Imager (OLI) in terms of channel reflectance and normalized vegetation indices [7], [8]. Accordingly, there is a need to define quantitative transformations between Landsat sensors to ensure a long-term archive with consistency [7], [9], especially for the time-series analyses. For between-sensor transformation, the linear model through ordinary least-squares (OLS) regression was generally used as a simple and readily applicable way [7]–[10]. Meanwhile, paired observations synchronously acquired by different sensors are usually inaccessible for the investigations on comparison and transformation. To overcome the difficulty in collecting the paired acquisitions, synthesizing broadband multispectral records from hyperspectral profiles (i.e., from Hyperion) were proven as a feasible way [9]–[17].

Inclusion of the MSS in Landsat time-series analyses, considering its historical importance, will ideally benefit the reconstruction of Earth's surface history back to 1972. Without comprehensive inclusion of the MSS archive, the entire power and benefits of the Landsat program are not fully realized [2], [18], [19]. The Landsat 1–5 MSS archive reprocessed has been available in the Landsat Collection 1 Level-1 data product since May 2018, being particularly for areas over North America, East Asia, and Australia (please refer to https://landsat.usgs.gov/usgs-landsat-global-archive). Fig. 2 shows the number of valid Landsat MSS scenes for a specific area. For this specific area, the archived MSS data may make time-series analyses of Landsat observations further extend to the 1970s. However, applications and investigations of the Landsat MSS archival images have been still relatively limited although with an increasing trend since the open data policy implemented in 2008 [18]–[26] compared with its successors, such as Thematic Mapper (TM), ETM+, and OLI [6]. Accordingly, for regions with valid MSS archival data, investigations are necessary.

Detailed investigations on the characterization of the Landsat 1–5 MSS for consistency issues have not been performed previously. This article attempts to investigate, comprehensively, the characterization and comparison of the Landsat 1–5 MSS in terms of channel reflectance and derived spectral indices and features. Furthermore, to make the comparability of observations, and of derived variables, practical transformation models are investigated. Factors mainly challenging the continuity between the Landsat MSS and other successive sensors are discussed. Accordingly, it intends to show comprehensive insights on the characterizations of the Landsat 1–5 MSS and to call attention to the inclusion of the MSS archive in time-series analyses. The rest of this article is organized as follows. Section II details the method. Data are described in Section III. Results on between-sensor comparison and transformation are shown in Section IV. Discussion and conclusion are presented in Sections V and VI, respectively.

II. METHODS

Due to the difficulty in collecting substantial contemporaneous observations of the Landsat MSS, a synthesized data collection generated from Hyperion hyperspectral profiles was
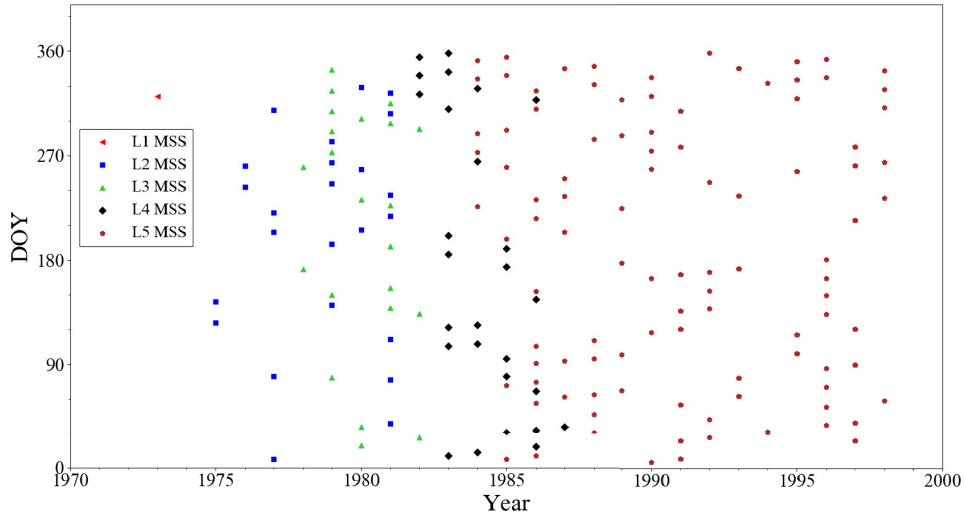
Fig. 2. Acquisition day-of-year (DOY) of all valid MSS archival scenes in the Landsat Collection 1 Level-1 data product over the Worldwide Reference System (WRS)-2 Path/Row 123/032 (for the Landsat 4-5 MSS), considering an overlap with the WRS-1 Path/Row 133/032 (for the Landsat 1-3 MSS), during 1973–1998. The valid scene was determined in terms of cloud cover and visual appearance (i.e., no cloud covering the urban areas of interest) and freely accessed at EarthExplorer (https://earthexplorer.usgs.gov/).

used in this article. The capability of Hyperion to synthesize the broadband multispectral channels (e.g., ETM+) was proven and employed previously [9]–[17].

Characterization differences among the Landsat 1–5 MSS were mainly shown through the comparisons of channel effective wavelength and reflectance, followed by derived vegetation spectral indices and the Tasseled Cap (TC) transformed features [18], [27]. Specifically, two widely used vegetation spectral indices were discussed, the Normalized Difference Vegetation Index (NDVI) [28] and the Enhanced Vegetation Index with a modified version (EVI) [29], which are the key variables in Landsat higher level science products [30]. The discussion on NDVI and EVI for the Landsat MSS will benefit the continuity of the Landsat higher level science products and will facilitate the full use of the Landsat MSS archive.

A. Channel Effective Wavelength and Reflectance

As an important indicator of channel characterization [31]–[33], the effective wavelength calculated for individual channels of the Landsat 1–5 MSS is

$$\lambda_{\text{eff\_Bi}}^{\text{L}} = \frac{\int_{\lambda_{\text{BiS}}^{\text{L}}}^{\lambda_{\text{BiE}}^{\text{L}}} \lambda \text{SRF}_{\text{Bi}}^{\text{L}}(\lambda) d\lambda}{\int_{\lambda_{\text{BiS}}^{\text{L}}}^{\lambda_{\text{BiE}}^{\text{L}}} \text{SRF}_{\text{Bi}}^{\text{L}}(\lambda) d\lambda} \quad (1)$$

where $\text{SRF}_{\text{Bi}}^{\text{L}}(\lambda)$ is the spectral response function (SRF) of a specific channel Bi, while $\lambda_{\text{BiS}}^{\text{L}}$ and $\lambda_{\text{BiE}}^{\text{L}}$ are the start wavelength and end wavelength, respectively. $\lambda_{\text{eff\_Bi}}^{\text{L}}$ is the effective wavelength for the channel Bi, which was obtained in this article through the "Trapezoid" strategy [32], [33]. The superscript "L" stands for the Landsat MSS.

Meanwhile, the synthesized reflectance for channel Bi ($\text{Ref}_{\text{Bi}}^{\text{L}}$) of the Landsat MSS is estimated as an effective

reflectance over its spectral range, as follows:

$$\text{Ref}_{\text{Bi}}^{\text{L}} = \frac{\int_{\lambda_{\text{BiS}}^{\text{L}}}^{\lambda_{\text{BiE}}^{\text{L}}} \text{Ref}^{\text{H}}(\lambda) \text{SRF}_{\text{Bi}}^{\text{L}}(\lambda) d\lambda}{\int_{\lambda_{\text{BiS}}^{\text{L}}}^{\lambda_{\text{BiE}}^{\text{L}}} \text{SRF}_{\text{Bi}}^{\text{L}}(\lambda) d\lambda} \quad (2)$$

where $\text{Ref}^{\text{H}}(\lambda)$ is the reflectance value of a calibrated Hyperion profile at a specific wavelength λ. The superscript "H" stands for the Hyperion profile. The Hyperion profile is the surface reflectance spectrum after atmospheric correction (see Section III-B). To solve (2), procedures performed are the weights' calibration (3), the weights normalization (4), and the weighted sum (5), which is a modified version for the synthesized reflectance in (2) [9]–[11], [14]

$$W_{\text{i}}^{\text{H}} = \int_{\lambda_{\text{iS}}}^{\lambda_{\text{iE}}} \text{SRF}_{\text{i}}^{\text{H}}(\lambda) \text{SRF}_{\text{Bi}}^{\text{L}}(\lambda) d\lambda \quad \text{when } \lambda_{\text{iC}}^{\text{H}} \in \left(\lambda_{\text{BiS}}^{\text{L}}, \lambda_{\text{BiE}}^{\text{L}} \right)$$

$$(3)$$

$$nW_{\text{i}}^{\text{H}} = \frac{W_{\text{i}}^{\text{H}}}{\sum_{\text{i}} W_{\text{i}}^{\text{H}}} \quad (4)$$

$$\text{Ref}_{\text{Bi}}^{\text{L}} = \sum_{\text{i}} \left(nW_{\text{i}}^{\text{H}} \cdot \text{Ref}_{\text{i}}^{\text{H}} \right) \quad (5)$$

where $\text{SRF}_{\text{i}}^{\text{H}}(\lambda)$ and $\text{Ref}_{\text{i}}^{\text{H}}$ are the SRF and reflectance for the Hyperion channel i, respectively, while W_{i}^{H} and nW_{i}^{H} are the weight and the normalized weight correspondingly. In (3), λ_{iS} and λ_{iE} are the start wavelength and end wavelength of the Hyperion channel i. As shown in (5), $\text{Ref}_{\text{Bi}}^{\text{L}}$ is obtained as a weighted sum of all valid Hyperion channels in which the center wavelengths ($\lambda_{\text{iC}}^{\text{H}}$) are located within the spectral range of the MSS channel Bi. The SRF for the Hyperion ($\text{SRF}_{\text{i}}^{\text{H}}(\lambda)$) was estimated through (16) (see Section III-A), as in previous investigations [9], [10].

B. Between-Sensor Comparison

In addition to the channel effective wavelength, the between-sensor comparison of the Landsat 1–5 MSS was discussed,

in terms of channel reflectance, derived vegetation spectral indices (i.e., NDVI and EVI), and two features (i.e., brightness and greenness) obtained through the TC transformation [27].

Vegetation spectral indices extracted from remote sensing have been widely used to delineate vegetation characteristics and monitor land surface dynamics [29], [33]–[39]. Two widely used vegetation spectral indices were discussed, including NDVI (6) and a two-band EVI [EVI2, (7)]. EVI provides improved sensitivity in high biomass regions while minimizing soil and atmosphere influences [29]. Compared with the original EVI developed for sensors with the Blue channel in addition to the red and NIR channels [40], the EVI2 was proposed for sensors without the Blue channel [29]

$$\text{NDVI} = \frac{(\text{Ref}_{\text{nir}} - \text{Ref}_{\text{red}})}{(\text{Ref}_{\text{nir}} + \text{Ref}_{\text{red}})} \quad (6)$$

$$\text{EVI2} = 2.5 \times \frac{(\text{Ref}_{\text{nir}} - \text{Ref}_{\text{red}})}{(\text{Ref}_{\text{nir}} + 2.4\text{Ref}_{\text{red}} + 1)} \quad (7)$$

where Ref_{red} and Ref_{nir} are the channel reflectance over red and NIR regions, respectively. The NIR1 (700–800 nm) channel was used in vegetation indices estimation. Descriptions of the channels are presented in Fig. 1 and Table I.

Meanwhile, the TC transformation initially proposed in [27] provides a way to generate spectral features, which can be readily interpretable and are directly associated with the physical parameters of the land surface, and to reduce data volume with minimal information loss [41]. The spectral features derived from the TC transformation have been widely used for land surface mapping [42]–[44]. Corresponding versions of the TC transformation have been developed for all Landsat sensors, including the MSS [27], the TM [41], the ETM+ [45], and the OLI [46]. Particularly, for the MSS, two readily interpretable features through the TC transformation are brightness and greenness [27]. The brightness as a weighted sum of all MSS channels measures the total reflection performance. Meanwhile, the greenness measures the reflectivity contrast between two NIR channels and two visible channels (i.e., green and red), which is considered a good indicator for vegetation [41]. Currently, TC transformation for the MSS is only available to digital number (DN) records [18], [27]. The development of reflectance-based TC transformation for the MSS is valuable; however, it is beyond the scope of this article. To obtain DN from the channel reflectance (the synthesized data), procedures used are the following equations:

$$L^s_{\text{Bi}} = \text{Ref}^L_{\text{Bi}} \cdot (\text{ESUN}_{\text{Bi}} \cdot \cos(\theta_s))/(\pi \cdot d^2) \quad (8)$$

$$\text{DN}_{\text{Bi}} = (L^s_{\text{Bi}} - \text{bias}_{\text{Bi}})/\text{gain}_{\text{Bi}} \quad (9)$$

where θ_s is the solar zenith angle, and d is the Earth-to-Sun distance, which is in astronomical units (from about 0.9833 to 1.0167) [47], while ESUN_{Bi} is the exoatmospheric solar irradiance (ESUN) in spectral channel Bi. The cosine of the solar zenith angle is equal to the sine of the solar elevation. We set $d = 1$ (astronomical unit) and solar elevation $= 60°$ to facilitate the DN calculation. The gains (gain_{Bi}) and biases (bias_{Bi}) associated with radiometric calibration for respective MSS sensors [18] and the ESUN values for the Landsat 5 MSS [18], [47] were used.

C. Measures for Between-Sensor Difference

The relative difference (RD) measures the individual between-sensor difference of sample (pair) j, for the corresponding variable (Var_i), which is defined as

$$\text{RD}^{\text{L(N)}}_{ij} = 2 \times \frac{\left(\text{Var}^{\text{L(N)}}_{ij} - \text{Var}^{\text{L5}}_{ij}\right)}{\left(\text{Var}^{\text{L(N)}}_{ij} + \text{Var}^{\text{L5}}_{ij}\right)} \times 100 \quad (10)$$

where $\text{Var}^{\text{L(N)}}_{ij}$ and $\text{Var}^{\text{L5}}_{ij}$ are the corresponding values of sample j ($j = 1, 2, \ldots, nn$, while nn is the number of sampling pairs to be compared) for the variable Var_i of the Landsat (N) MSS ($N = 1, 2, 3, 4$) and the Landsat 5 MSS (as the baseline or reference), respectively.

To measure the overall between-sensor difference, three indicators considered were the mean difference (MD), the root mean square deviation (RMSD), and the mean RD (MRD)

$$\text{MD}^{\text{L(N)}}_i = \text{mean}\left(\text{Var}^{\text{L(N)}}_{ij} - \text{Var}^{\text{L5}}_{ij}\right) \quad (11)$$

$$\text{RMSD}^{\text{L(N)}}_i = \text{sqrt}\left(\text{mean}\left(\left(\text{Var}^{\text{L(N)}}_{ij} - \text{Var}^{\text{L5}}_{ij}\right)^2\right)\right) \quad (12)$$

$$\text{MRD}^{\text{L(N)}}_i = \text{mean}\left(\text{RD}^{\text{L(N)}}_{ij}\right) \quad (13)$$

where mean() and sqrt() are the procedures used to get the mean value and the square root value, respectively.

These indicators were used in the previous investigations [7], [10]. To measure the average RD in vegetation indices and the TC transformed greenness, the median RD (MdRD) was used. Compared with the MRD, the MdRD is less affected by extreme cases. Meanwhile, respective variables for the Landsat 5 MSS were used as references in between-sensor comparison.

$$\text{MdRD}^{\text{L(N)}}_i = \text{median}\left(\text{RD}^{\text{L(N)}}_{ij}\right) \quad (14)$$

where median() is used to get the median value.

D. Between-Sensor Transformation

The linear model was applied, as adopted previously [7]–[10], to make the observation continuity between different sensors

$$\text{Var}^{\text{L5}}_i = \text{Slope}^{\text{L(N)}}_{\text{Var}_i} \times \text{Var}^{\text{L(N)}}_i + \text{Offset}^{\text{L(N)}}_{\text{Var}_i} \quad (15)$$

where $\text{Slope}^{\text{L(N)}}_{\text{Var}_i}$ and $\text{Offset}^{\text{L(N)}}_{\text{Var}_i}$ are the linear transformation model parameters for the corresponding variable Var_i of the Landsat (N) MSS ($N = 1, 2, 3, 4$), obtained using the Landsat (N) MSS regressed against the Landsat 5 MSS correspondingly.

OLS regression was usually used to solve the linear transformation model by minimizing the summed square of the residuals. OLS regression can get the best-unbiased estimators, given that the residual has a constant variance called homoscedasticity. However, suspectable estimates are likely obtained when the heteroscedastic data are analyzed. Effects of heteroscedasticity on OLS estimates were investigated, by comparing against the estimates through weighted least-squares (WLS) regression that served as a common method

for the heteroscedasticity issue (see Section V-C). The comparison suggested that the estimates obtained through OLS regression were acceptable although they showed relatively larger confidence intervals (see Table V).

Furthermore, uncertainties and improvements associated with the transformation model were demonstrated through a cross-validation strategy. The cross-validation is a proper way to assess model prediction performance. Same as in previous investigations [9], [10], the K-fold cross-validation ($K = 5$) with 10 000 simulations was performed. For each validation case, the mean (or median) RDs (MRD or MdRD) after and before transformation were measured, respectively, and compared. Meanwhile, the uncertainty of the transformation model was presented by the distribution of the model estimates.

III. DATA

A. Spectral Response Function

The channel-average spectral response functions of the Landsat 1–5 MSS are publicly available at https://landsat.gsfc. nasa.gov due to the efforts made by the Image Processing Lab, South Dakota State University. In particular, the SRFs for the Landsat 1–3 MSS were digitized from the plots in contractor reports, which were sampled at 1 nm steps. It is estimated an uncertainty with ±3 nm on the wavelength samples. The SRFs for the Landsat 4–5 MSS were digitized from considerably better copies [48]. Compared with the SRFs for the predecessors, the SRFs for the Landsat 4–5 MSS were digitized at the tests' native spectral sampling, specifically at 10 nm for the green, red, and NIR1 channels, while at 20 nm for the NIR2 channel (https://landsat.gsfc.nasa. gov/spectral-response-of-the-multispectral-scanner-system-in-band-band-average-relative-spectral-response/). To facilitate the effective wavelength estimation and channel reflectance calculation, the SRFs for all channels of the Landsat 4–5 MSS were interpolated to 1-nm spectral resolution using the spline method, as in [10] and [33]. Possible uncertainty associated with the choice of interpolation methods was discussed (see Section V-A).

The Hyperion SRFs are not publicly accessible. In this article, a Gaussian function was adopted to model the Hyperion SRFs, using the full-width at half-maximum (FWHM) and the center wavelength (16), as in [7]–[10]. The simulated Hyperion SRFs, recorded with a spectral resolution of 1 nm, were used subsequently in synthesizing the broadband reflectance of MSS

$$\text{SRF}_i^H(\lambda) = \exp\left(-\frac{4\ln(2)\left(\lambda - \lambda_{iC}^H\right)^2}{(\text{FWHM}_i)^2}\right) \quad (16)$$

where FWHM_i is the FWHM of the Hyperion channel i. The center wavelength and the FWHM are publicly available at https://archive.usgs.gov/archive/sites/eo1.usgs.gov/hyperioncoverage.html (accessed on February 28, 2020).

B. Hyperion Spectra Collection

As a primary instrument onboard the EO-1 spacecraft launched in November 2000, the Hyperion instrument was the first imaging spectrometer, acquiring data from space [49]. The Hyperion instrument is a high-resolution hyperspectral imager with 220 unique spectral channels, which approximately covers 400–2500 nm. Generally, each channel of Hyperion is characterized by an approximate 10-nm FWHM and with a spatial resolution of 30 m. There are only 196 unique channels calibrated in the Level-1 radiometric product due to detectors' low responsivity and overlap between channels (https://eo1.usgs.gov). The calibration of Hyperion was radiometrically stable to within 5% over the visible and NIR regions [49], [50]. The Hyperion profile, as actual observed surface condition, provides a valuable and unique data source to investigate the radiometric comparison between instruments [17]. The capability of Hyperion to synthesize the broadband multispectral channels has been proven [9]–[17]. A total of 10 000 calibrated Hyperion hyperspectral profiles, collected elaborately while maintaining spectra variability [16], [17], were used (see Fig. 3). These samples were selected from 158 Hyperion scenes through a two-step clustering procedure, which was atmospherically corrected using the 6S model (Second Simulation of the Satellite Signal in the Solar Spectrum) supplied with atmospheric products of Moderate Resolution Imaging Spectroradiometer (MODIS) [17]. This collection was used previously for between-sensor comparison and transformation [9], [10], [16], [17]. Anomalous (negative) channel reflectance values were observed in several Hyperion spectra, especially for the channels located in 1326–1427 and 1830–1932 nm [10], which likely resulted from atmospheric impacts and improper correction. Nevertheless, considering the spectral range of the Landsat MSS (see Table I and Fig. 1), effects of the negative value in several Hyperion spectra on channel reflectance estimation of the Landsat MSS are assumed minor in this article.

IV. RESULTS

A. Channel Characterization of the Landsat MSS

Compared with the Landsat 1–3 MSS, the Landsat 4 MSS shows more similarities with the Landsat 5 MSS in the channel characterizations on average, including in spectral response function (see Fig. 1) and in effective wavelength (see Table II). Significant discrepancies in the spectral response function between sensors are observed, especially for the NIR channels. The discrepancy around the end wavelength of NIR2 is possibly associated with the extraction method for the NIR2 SRF of the Landsat 4–5 MSS (see Fig. 1). The NIR2 SRF currently available was extracted through an extrapolation, which made a value close to zero at 1140 nm (https://landsat.gsfc.nasa.gov). The significant difference is shown between Landsat 3 and Landsat 5, among others, especially for the NIR channels (i.e., NIR1 and NIR2) (see Fig. 1). In addition to its association with the sensor, the difference in effective wavelength (using the Landsat 5 MSS as reference) varies with the channel. The difference of the Landsat 2 MSS in effective wavelength for the red channel is about 11 nm, and the difference is nearly 5 nm for the NIR1 channel (see Table II). The variations of the channel characterizations likely contribute a lot to the differences in reflectance and derived spectral indices

This article has been accepted for inclusion in a future issue of this journal. Content is final as presented, with the exception of pagination.

6   IEEE TRANSACTIONS ON GEOSCIENCE AND REMOTE SENSING
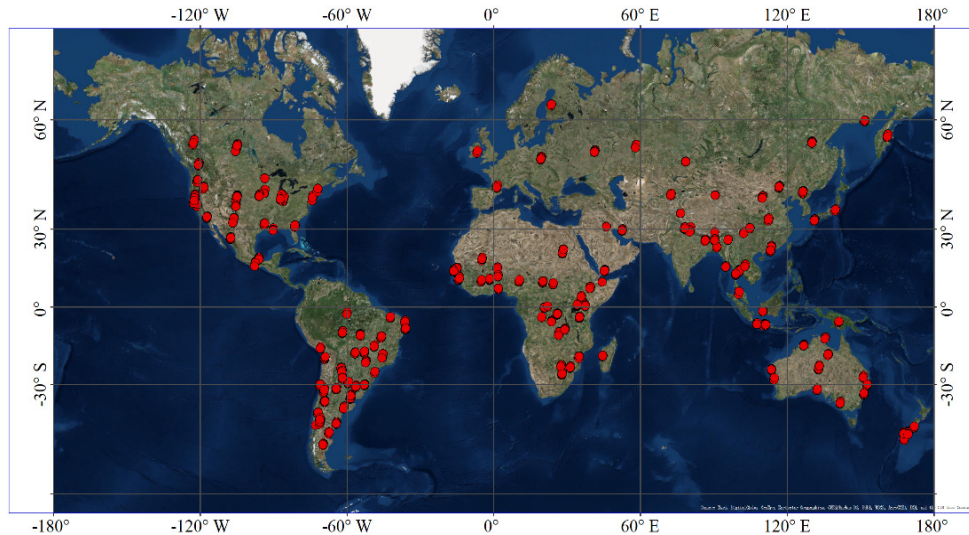

Fig. 3. Spatial distribution of the Hyperion spectra profiles (red dots) included in the collection used for reflectance simulation. The profiles are geographically overlapped or approximate, with some not being visible due to the enlarged symbols. Details on the Hyperion spectra selection are presented in [17].

TABLE II
CHANNEL EFFECTIVE WAVELENGTH (nm) OF THE LANDSAT 1–5 MSS

	Green	Red	NIR1	NIR2
Landsat 1	553.012	653.235	748.661	913.595
Landsat 2	549.973	660.793	751.963	910.364
Landsat 3	545.298	655.421	743.509	908.389
Landsat 4	550.712	650.281	754.212	926.965
Landsat 5	552.748	649.564	756.575	931.126

between the Landsat sensors [9], [33], [51]. Accordingly, a specific transformation model for each corresponding channel of respective sensors is required to make the consistency of the Landsat 1–5 MSS archive.

B. Difference in Channel Reflectance

In the spectra collection (including 10 000 samples), most samples are characterized with low reflectance (i.e., less than 0.15) in the green channel and the red channel, while the reflectance over the NIR region (i.e., the NIR1 and NIR2 channels) is mainly located from 0.20 to 0.30 (see Fig. 4). The distribution difference is relatively significant for the red channel and the NIR1 channel. As shown in Fig. 4, the obvious differences (greater than 2%) are observed for the red channel and the NIR1 channel, whereas the frequency difference is within ±1% for the green channel and the NIR2 channel. Generally, the between-sensor difference is more visible for the Landsat 2–3 MSS, while the slight difference is recorded for the Landsat 4 MSS (see Fig. 4). Furthermore, the statistics of the Jarque–Bera test [52] showed that all respective collections of channel reflectance did not come from a normal distribution at the 0.05 significance level. Accordingly, the Wilcoxon signed-rank test as a nonparametric method was further used in the comparison test of channel reflectance. Findings show that the between-sensor differences

in reflectance are significant, respectively (at the 0.05 significance level).

Negatively significant overall between-sensor differences are observed for the NIR1 channel, whereas intermediate and positive overall between-sensor differences are shown for the red channel (see Table III). In particular, the Landsat 2 MSS has the greatest MD of 0.006 for the red channel, while the Landsat 3 MSS has the greatest MD of −0.010 for the NIR1 channel. The RMSD of channel reflectance is more significant for the NIR1 channel and is generally smaller for the green channel. According to the MRD, the overall between-sensor difference is relatively obvious for the red channel and the NIR1 channel although it varies with sensors. As a whole, the between-sensor disagreement is more visible for the Landsat 3 MSS, as it has obvious MRD (−4.776%) for the NIR1 channel and intermediate MRDs for the green channel and the red channel. The overall between-sensor difference is also obvious for specific channels of other sensors. For example, the MRDs for the red channel of Landsat 2 and the NIR1 channel of Landsat 1 are 6.270% and −3.089%, respectively. Moreover, the overall RDs in channel reflectance vary with sensors, which are also channel-related (see Fig. 5). It appears that the Landsat 4 MSS and the Landsat 5 MSS are generally comparable as the overall RDs mainly locate around zero (within ±2%). Between-sensor comparability is also shown for the green channel and the NIR2 channel, with the overall RDs mainly falling within ±5%. By contrast, the overall RDs are notable for the red channel and the NIR1 channel, especially for the Landsat 2–3 MSS.

C. Difference in Derived Spectral Indices and Features

Between-sensor differences in reflectance of individual channels are especially important when considering derived spectral indices, which usually depends on the reflectivity contrast between channels (e.g., NDVI) [9], [33], [51]. Compared with the differences of individual channels (i.e., the red

This article has been accepted for inclusion in a future issue of this journal. Content is final as presented, with the exception of pagination.

CHEN *et al.*: CHARACTERIZATION OF MSS CHANNEL REFLECTANCE AND DERIVED SPECTRAL INDICES　　　　　　　7
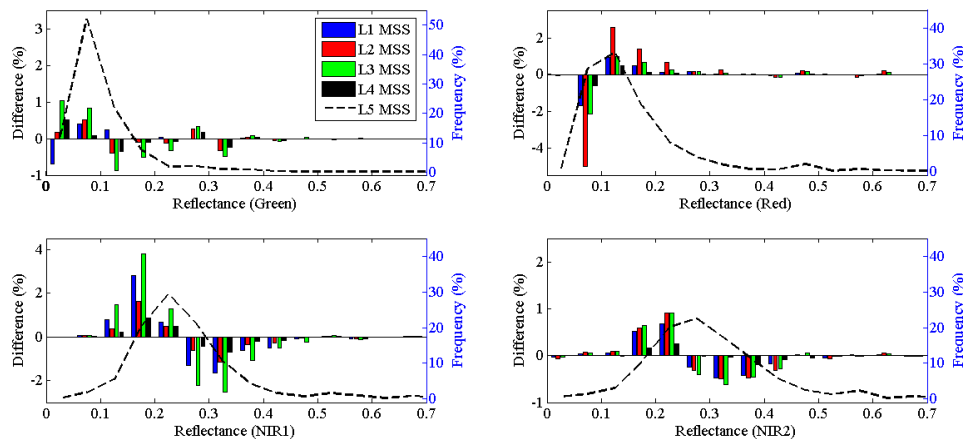

Fig. 4. Distribution of channel reflectance and the corresponding differences for the Landsat 1–4 MSS, using the Landsat 5 MSS as reference. Results are based on simulations using a collection of Hyperion hyperspectral spectra, as surface reflectance atmospherically corrected (totally 10 000 samples). The dashed line shows the distribution of the Landsat 5 MSS. For all plots, the bin size is 0.05, while the *X*-axis range is set as (0, 0.70) within which 99.50% samples are located to show the between-sensor difference clearly.

TABLE III

DIFFERENCE MEASURES FOR CHANNEL REFLECTANCE AND THE DERIVED SPECTRAL FEATURES USING
CORRESPONDING VARIABLE OF THE LANDSAT 5 MSS AS REFERENCE

		Green	Red	NIR1	NIR2	NDVI[a]	EVI2	Brightness	Greenness
MD	Landsat 1	3.45e-4	0.002	-0.007	-0.002	-0.020	-0.015	-0.546	-1.028
		(5.61) [c]	(-9.60)	(3.11)	(-15.72)				
	Landsat 2	-8.81e-4	0.006	-0.004	-0.002	-0.031	-0.018	0.133	-1.247
		(-6.80)	(4.93)	(5.98)	(-7.08)				
	Landsat 3	-0.003	0.003	-0.010	-0.002	-0.030	-0.022	-1.184	-1.426
		(-3.41)	(0.82)	(-4.18)	(0.04)				
	Landsat 4	-8.56e-4	4.50e-4	-0.002	-6.58e-4	-0.006	-0.005	-0.314	-0.370
		(1.13)	(-4.79)	(6.29)	(-7.79)				
RMSD	Landsat 1	5.10e-4	0.002	0.009	0.003	0.025	0.019	1.210	1.398
		(6.00)	(9.64)	(8.23)	(17.98)				
	Landsat 2	0.002	0.006	0.006	0.004	0.037	0.022	0.441	1.517
		(6.98)	(5.45)	(6.69)	(7.38)				
	Landsat 3	0.004	0.003	0.014	0.004	0.035	0.027	1.595	1.910
		(3.91)	(1.04)	(5.69)	(1.74)				
	Landsat 4	0.001	5.62e-4	0.003	9.58e-4	0.007	0.006	0.494	0.953
		(1.31)	(5.53)	(6.83)	(8.47)				
MRD[b] (%)	Landsat 1	0.500	2.297	-3.089	-0.657	-7.456	-9.348	-1.840	-9.417
		(21.00)	(-42.26)	(9.31)	(-21.37)	[-7.101]	[-8.583]		[0.200]
	Landsat 2	-0.703	6.270	-1.833	-0.897	-11.268	-11.524	0.361	-11.141
		(-36.87)	(17.50)	(11.47)	(-11.31)	[-10.920]	[-11.153]		[-5.017]
	Landsat 3	-2.470	2.977	-4.776	-0.863	-11.461	-14.228	-3.426	-13.668
		(-14.23)	(3.05)	(-4.64)	(2.00)	[-11.742]	[-14.153]		[-8.783]
	Landsat 4	-0.825	0.591	-1.024	-0.245	-2.140	-2.771	-0.684	-2.803
		(4.62)	(-13.34)	(8.80)	(-11.23)	[-1.624]	[-2.152]		[-3.735]

[a]The NIR1 channel was used for the estimations of NDVI and EVI2 in this paper.
[b]For NDVI, EVI2, and Greenness, the median relative difference (MdRD, (14)) was used for analysis, with the mean relative difference (MRD, (13)) being listed in [ ] as supplementary. The TC transformed features (Brightness and Greenness) of MSS were based on digital number (DN) records estimated from channel reflectance correspondingly through (8) and (9), of which the related parameters for MSS were presented in [18] and [47].
[c]Measures in ( ) were the between-sensor differences based on DN records.

channel and the NIR1 channel), the differences of the derived spectral indices (i.e., NDVI and EVI2) are larger (see Table III). Taking the Landsat 3 MSS as an example, the MDs for NDVI and EVI2 are -0.030 and -0.022, respectively, which are obviously greater than the corresponding MDs for the red channel (0.003) and the NIR1 channel (-0.010). Because the same channels were used for NDVI and EVI2, the between-sensor differences in the vegetation indices are similar for the MSS, respectively. As mentioned earlier, the between-sensor differences for the red channel and the NIR1 channel are positive and negative, respectively, which alleviates the reflectance contrast followed by the decrease in vegetation indices. Accordingly, compared against the reference (i.e., Landsat 5 MSS), on average, the Landsat 1–4 MSS has negative biases in the vegetation indices (see Table III). Specifically, greater biases are observed for Landsat 2 and Landsat 3, while intermediate and small biases are presented for Landsat 1 and Landsat 4, respectively.
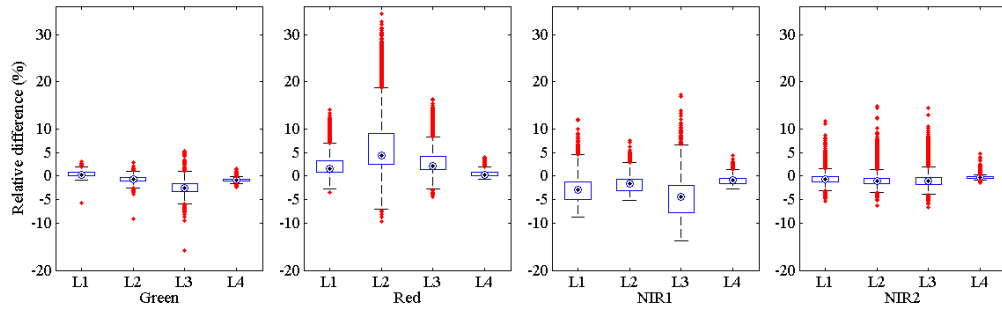
Fig. 5.   RDs of channel reflectance for the Landsat 1–4 MSS using the Landsat 5 MSS as reference. The box plot shows the difference distribution of the corresponding channel. The central mark is the median, and the bottom and top of the box are the 25th ($Q1$) and 75th percentiles ($Q3$), respectively. The distance between the top and bottom is the interquartile range (IQR, $Q3–Q1$). The whiskers are black lines extending values above and below the box, which are $Q3 + 1.5\text{IQR}$ and $Q1 − 1.5\text{IQR}$, respectively. Obvious differences are plotted individually as red points, locating outside the range determined by the whiskers.
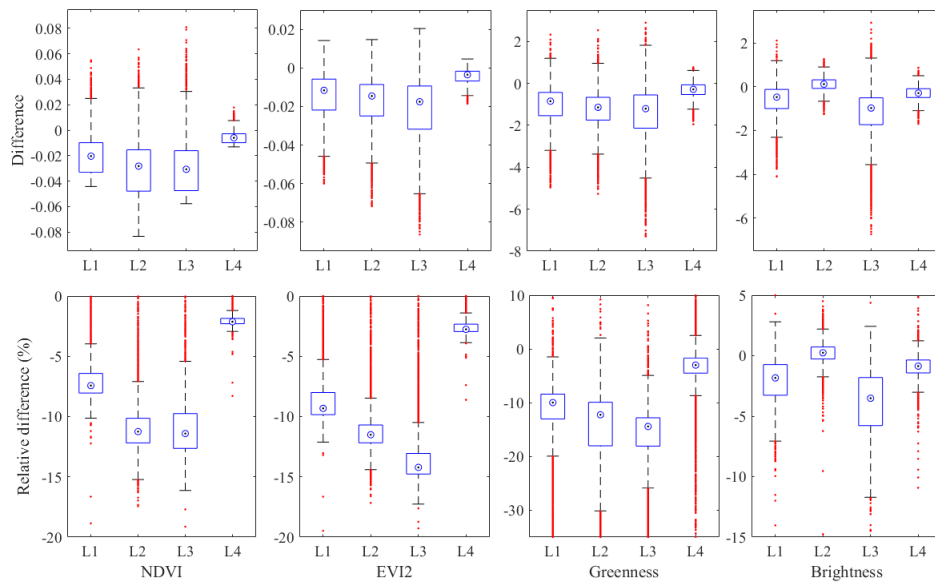
Fig. 6.   (Top) Differences and (Bottom) RDs for the vegetation indices (NDVI and EVI2) and the TC transformed features (greenness and brightness) of the Landsat 1–4 MSS, using the Landsat 5 MSS as reference. The box plot in this figure is similar as in Fig. 5. However, in the subplots of RD (Bottom), the Y-axis was truncated at $−20\%$ and 0% for NDVI and EVI2, $−35\%$ and 10% for the TC greenness, and $−15\%$ and 5% for the TC brightness to highlight the difference distribution of most samples. Several extreme RDs ($>50\%$) observed for NDVI, EIV2, and the TC greenness, respectively, are not shown.

The TC transformed features of the Landsat 1–4 MSS (except for the brightness of Landsat 2) show negative biases, as the vegetation indices do (see Table III). The mean (or median) RD (MRD or MdRD, in Table III) shows that the brightness insignificantly varies across sensors compared against the vegetation indices (i.e., NDVI and EVI2) and greenness. As mentioned, the TC transformation is done through a linear model with fixed parameters. Accordingly, while the DN-based biases are different (positive or negative) for individual channels of each MSS, spectral contrast is generally alleviated, resulting in negative bias in the greenness (see Table III). Considering the MdRD, between-sensor differences in vegetation indices and the TC greenness are similar. Nevertheless, it is worth noting that the between-sensor difference in the TC greenness linearly and directly relates to the biases in individual channels. Meanwhile, the difference in the normalized vegetation indices (e.g., NDVI and EVI2) shows

a more complicated relationship with the individual channel biases, which is regulated by actual (as reference) vegetation indices through a nonlinear manner.

Due to its similarity to Landsat 5 for the MSS individual channels, Landsat 4 has small between-sensor differences for the vegetation indices and for the TC transformed features although with varied and negative biases (see Fig. 6). The RDs are located around $−2.5\%$ for the vegetation indices and the TC greenness. By contrast, the between-sensor differences of Landsat 1–3 are relatively significant for the vegetation indices and the TC greenness. For example, the NDVI differences of Landsat 2 are mainly located from $−0.08$ to 0.04. A similar distribution of the EVI2 differences is observed although the EVI2 difference is generally smaller (see Table III and Fig. 6). Moreover, the RDs for the vegetation indices are more significant compared with the RDs for individual channels (see Table III and Figs. 5 and 6).

This article has been accepted for inclusion in a future issue of this journal. Content is final as presented, with the exception of pagination.

CHEN *et al.*: CHARACTERIZATION OF MSS CHANNEL REFLECTANCE AND DERIVED SPECTRAL INDICES
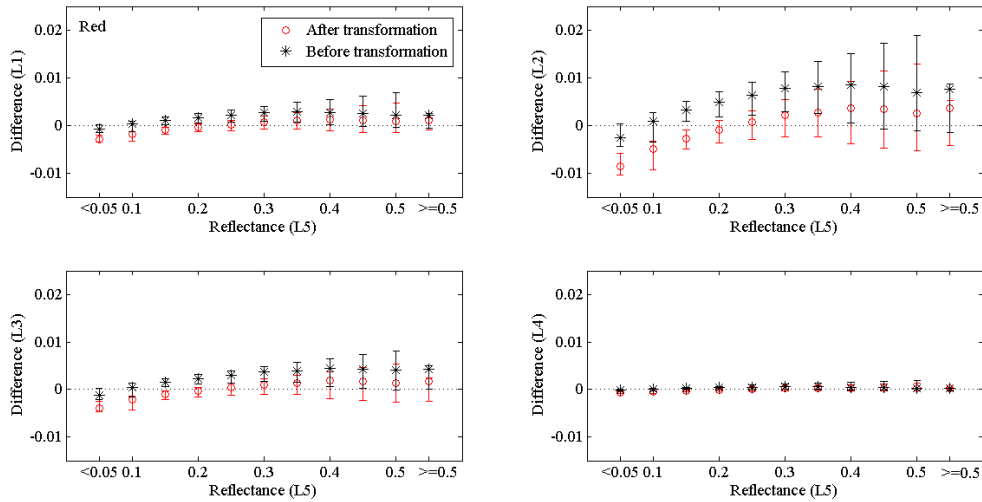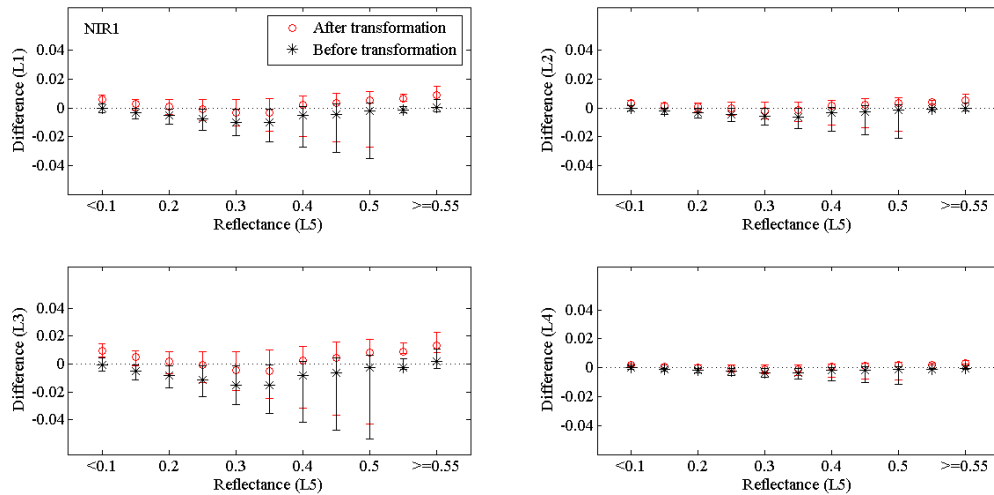
9

Fig. 7. Between-sensor differences after (red) and before (black) transformation for the red channel of the Landsat 1–4 MSS, using the Landsat 5 MSS as reference. The differences are shown by median (respective marks) and range (vertical lines) with the lower and upper taken as 5% and 95% percentiles for contiguous 0.05 reflectance ranges of the corresponding channel. All subplots in the figure are plotted using the same axis ranges.

Fig. 8. Between-sensor differences after (red) and before (black) transformation for the NIR1 channel of the Landsat 1–4 MSS, using the Landsat 5 MSS as reference.

The RDs for NDVI of the Landsat 3 MSS are mainly from −16% to −5% with the median about −11.5%, while those of the Landsat 2 MSS are mainly from −15% to −7%.

In summary, differences are observed for individual channels and derived variables, including vegetation indices and the TC transformed features (DN-based), across the Landsat 1–5 MSS. In terms of channel reflectance, there are major channel differences for the red and NIR1 channels. Meanwhile, overall comparability is observed for Landsat 4, and obvious disagreement is for Landsat 2 and Landsat 3, using Landsat 5 as reference. Generally, the biases in individual channels likely cause large biases in the normalized indices as a nonlinear form (i.e., NDVI and EVI2) (see Table III and Figs. 5 and 6). Accordingly, the normalized indices should be used with caution as the biases in individual channels can be amplified and generate more significant biases, which shows consistency with previous findings [9], [10], [33], [51], [53], [54]. Due to the spectral contrast alleviation, the TC transformed features (i.e., brightness and greenness) generally show smaller bias

compared with individual channels (see Table III), while more consistency between sensors possibly to be achieved through utilizing all channels [55].

D. Cross-Sensor Transformation to Improve Consistency Among the Landsat MSSs

Linear model, as a practical means for cross-sensor transformation [7]–[10], was applied to ensure the consistency between the Landsat MSSs. Considering the observed between-sensor differences and related effects on the bias in vegetation indices, the red channel and the NIR1 channel are mainly discussed further.

Overall, between-sensor comparability was improved through the linear transformation model, as shown by the decreases in between-sensor difference (see Figs. 7 and 8). However, the amplified differences after transformation are observable, mainly for samples with low reflectance. Specifically, for the Landsat 2 MSS red channel, the median

This article has been accepted for inclusion in a future issue of this journal. Content is final as presented, with the exception of pagination.

10   IEEE TRANSACTIONS ON GEOSCIENCE AND REMOTE SENSING
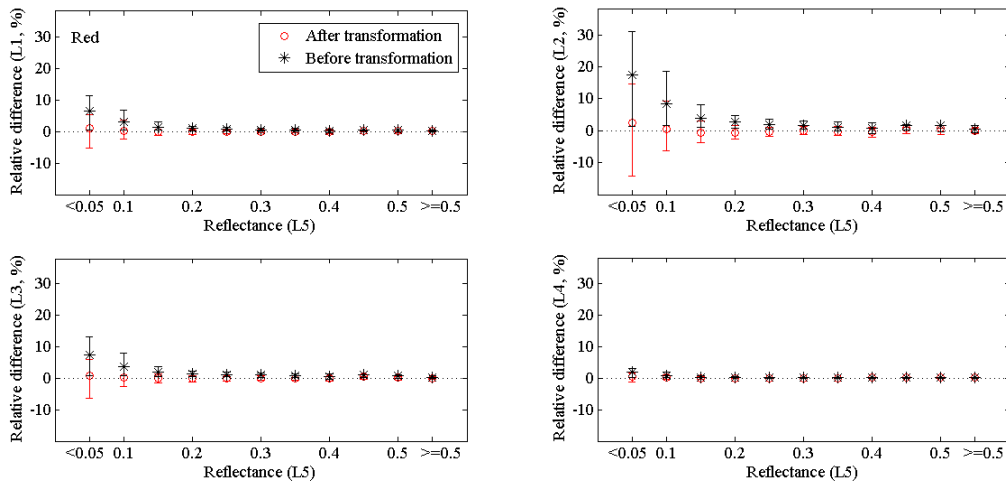

Fig. 9. Between-sensor RDs after (red) and before (black) transformation for the red channel of the Landsat 1–4 MSS, using the Landsat 5 MSS as reference.
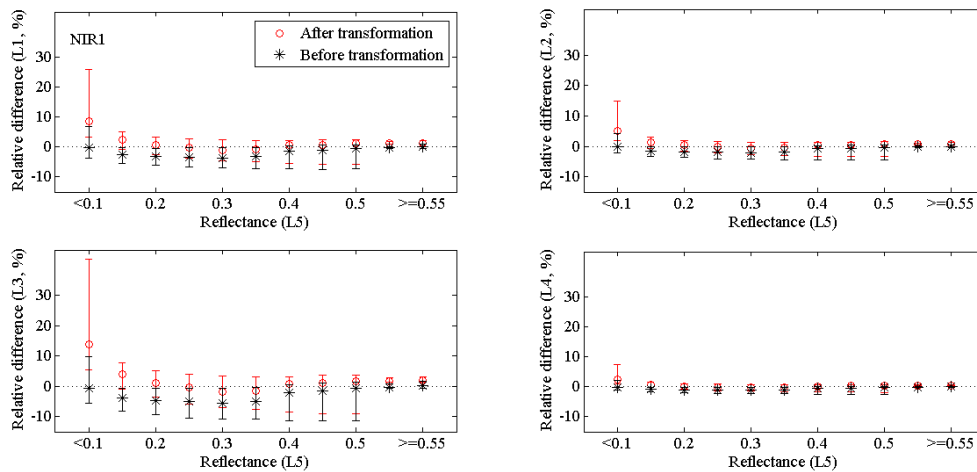

Fig. 10. Between-sensor RDs after (red) and before (black) transformation for the NIR1 channel of the Landsat 1–4 MSS, using the Landsat 5 MSS as reference.

between-sensor difference (negative) is amplified about 0.005 for samples with low reflectance (less than 0.10, with the proportion about 30%), whereas a decrease about 0.005 is observed over (0.20, 0.45) (see Fig. 7). The decreased RD (see Figs. 9 and 10) also suggests the improved between-sensor comparability of channel reflectance through a linear transformation. In particular, improvement for the red channel is significant, especially over low reflectance (less than 0.10). For the samples with low red reflectance, the decreases approximating 10% and 5% in median RD (positive) are observed for Landsat 2 and Landsat 3, respectively (see Fig. 9). As shown in Fig. 10, the RD for the NIR1 channel generally decreases for samples provided with moderate reflectance (0.10–0.50). However, the median RDs of Landsat 3 increase about 10% and 1.5% for the samples with low reflectance and high reflectance, respectively. RD for individual channels largely contributes to the biases in vegetation indices (i.e., NDVI and EVI2). Accordingly, the increased RD for the NIR1 channel over low reflectance (see Fig. 10) along with the improved

comparability of the red channel (see Fig. 9) results in a visible difference in the vegetation indices based on the transformed reflectance (see the "Channel transformation" in Fig. 15).

To investigate the effectiveness of transformation models for applications, the between-sensor differences in channel reflectance before and after transformation, respectively, were compared. Two pairs of MSS archived observations of Landsat 4 and Landsat 5 (over the WRS-2 Path/Row 123/032, see Fig. 2) with clear imagery were selected through carefully visual interpretation due, mainly, to uncertainties in the quality assessment (QA) band information (see Section V-E). The MSS observations without data problems visually (see Fig. 11) were freely accessed through EarthExplorer. In addition, several reflectively pseudoinvariant targets (i.e., the water body and airport) assumed were collected to estimate the observation differences associated with the interval between the paired MSS observations (with eight days). Comparisons and the difference measures for each pair of observations are based on 10 000 randomly selected samples (see Fig. 11). Consistency

This article has been accepted for inclusion in a future issue of this journal. Content is final as presented, with the exception of pagination.

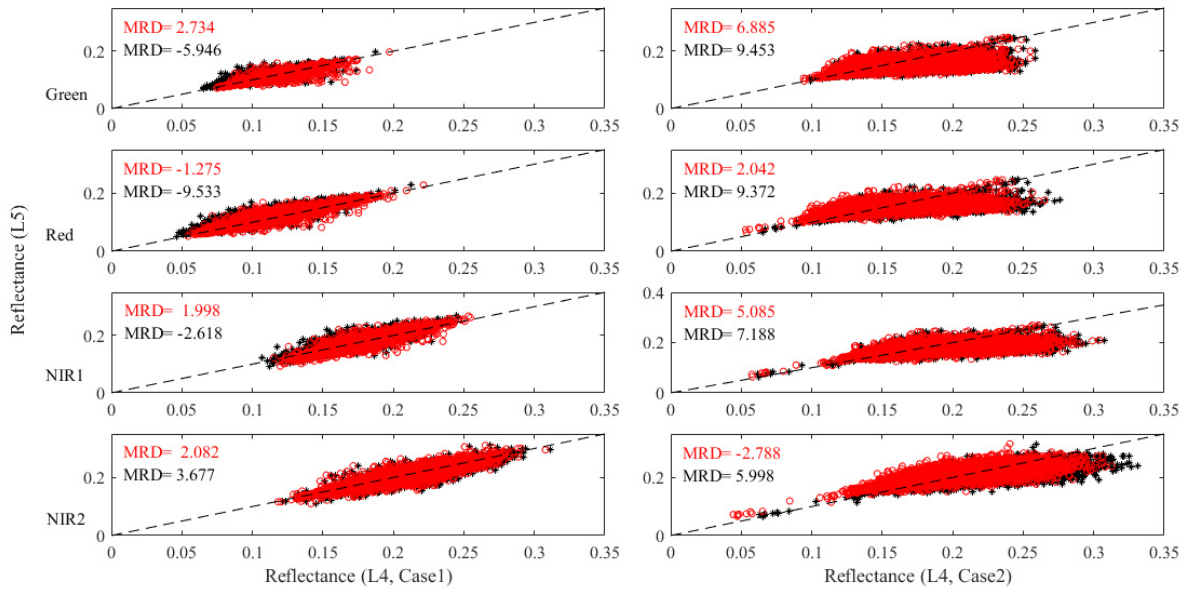CHEN *et al.*: CHARACTERIZATION OF MSS CHANNEL REFLECTANCE AND DERIVED SPECTRAL INDICES 11

Fig. 11. Channel reflectance comparisons of the samples randomly selected for two cases. (Left) Case 1. (Right) Case 2. In each scatter plot, the transformed channel reflectance (red circle) as well as the original channel reflectance (black asterisk) of the Landsat 4 (L4) MSS are shown with comparison against the corresponding channel reflectance of the Landsat 5 (L5) MSS. General differences measured by the MRD (13) before (black) and after (red) transformation are presented. The dashed lines are 1:1 lines superimposed for reference. Images used are LM04_L1TP_123032_19840925_20180410_01_T2 and LM05_L1TP_123032_19841003_20180411_01_T2 (for Case 1), and LM04_L1TP_123032_19841128_20180411_01_T2 and LM05_L1TP_123032_19841206_20180411_01_T2 (for Case 2).

of channel reflectance between the MSS observations of Landsat 5 and Landsat 4 is generally improved after transformation with an MRD decrease. The application cases verified the effectiveness of the transformation models generated through OLS regression, showing accordance with the findings based on cross-validation tests (see Figs. 9 and 10) and the previous investigations [7]–[10]. However, the difference measures of between-sensor vary between the two cases (see Fig. 11) and simulation dataset (see Table III), suggesting that other factors challenging the consistency of the Landsat MSS should be further considered and tackled in practice (see Section V-E).

V. DISCUSSION

A. Effect of Spectral Sampling Shift of the MSS SRF

For the SRFs of the Landsat 1–3 MSS, there is an estimated uncertainty with ±3 nm in wavelength samples (https://landsat.gsfc.nasa.gov). Potential errors in channel reflectance associated with the uncertainty of SRF were investigated. A shifted SRF was generated through shifting individual wavelength samples with an identical step (i.e., with 1 nm) while keeping its SRF value unchanged. Then, based on a shifted SRF, more estimation of channel reflectance was obtained when no shifts were performed to the Hyperion profile in channel reflectance estimation. Accordingly, six additional simulations with the shifts from −3 to 3 nm at an interval of 1 nm were generated. Based on the additional simulations, uncertainty in channel reflectance associated with the shifts was measured by the RD while using the original estimation (without shift) as the reference. Generally, compared with the between-sensor difference (see Table III), the reflectance variation resulted from the SRF shift is relatively

minor (see Fig. 12). In particular, for the Landsat 3 MSS, the median RDs associated with the NIR1 SRF shifts are proximately −1% to 0.5%, while the corresponding between-sensor difference is −4.776% (see Table III). Accordingly, the potential effect associated with the SRF uncertainty on the investigation was not considered.

B. Effect of Interpolation for the MSS SRF

Different methods for the SRF interpolation of the Landsat 4–5 MSS were compared, including linear interpolation, spline interpolation, and cubic interpolation. The effect associated with interpolations was measured by the variation coefficient, as the ratio of the standard deviation to mean (as a percent). Generally, the variation in channel reflectance caused by different interpolations of SRF is small, with the median variation coefficient being approximate to 0.02% for the Landsat 4 and 5 MSS channels (see Table IV). The interpolation methods show relatively significant effects on the red channel. However, for about 80% of samples, the variation of reflectance is less than 0.1%. Consequently, the interpolated SRFs for the Landsat 4–5 MSS with a spectral interval of 1 nm through the spline interpolation were used in reflectance simulation and effective wavelength estimation, as in previous investigations [9], [33].

C. Between-Sensor Transformation Models and Associated Improvements in Consistency

The transformation models of channel reflectance for the Landsat 3 MSS were discussed in detail to show models' reliability. Table V presents the model estimates obtained through OLS and WLS regressions separately. The coefficients
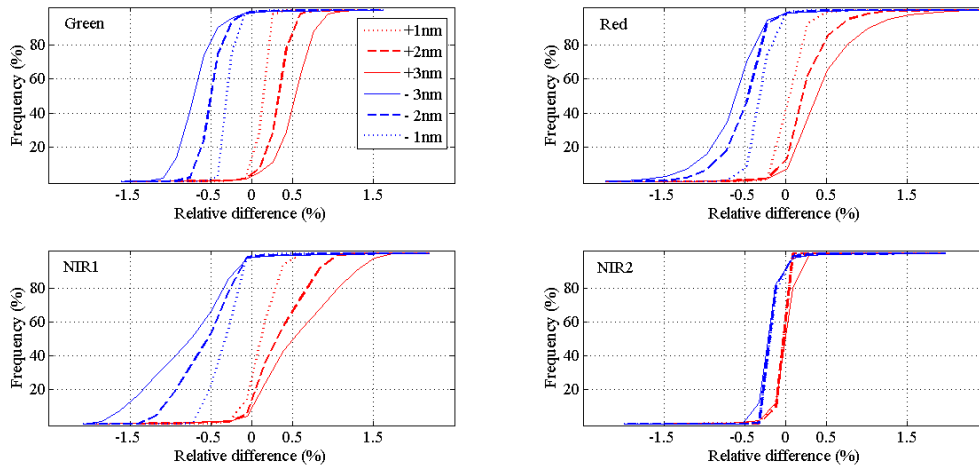
Fig. 12.   Effects of the SRF shifts of the Landsat 3 MSS (from −3 to 3 nm) on channel reflectance, measured by RD using the original simulation as reference.
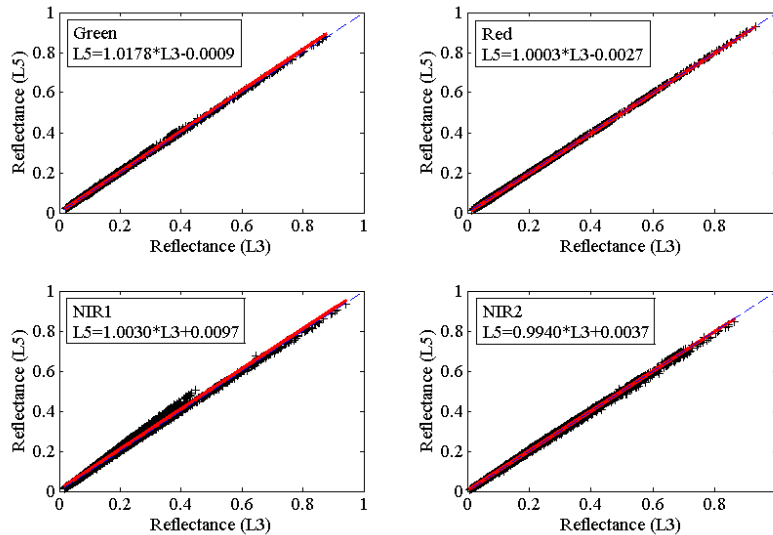

Fig. 13.   Demonstration of the linear transformation model through OLS regression for the Landsat 3 MSS. The red lines show regression of the Landsat 3 MSS against the Landsat 5 MSS for respective channels, while the transformation models are provided correspondingly. The dashed blue lines in all subplots are 1:1 lines superimposed for reference.

TABLE IV

EFFECTS OF INTERPOLATION METHODS ON CHANNEL REFLECTANCE OF THE LANDSAT 4–5 MSS

	Green (%)	Red	NIR1	NIR2
L4	**0.014**	**0.022**	**0.014**	**0.007**
	[0.003, 0.04]	[0.002, 0.299]	[0.001, 0.046]	[0.001, 0.065]
L5	**0.016**	**0.020**	**0.018**	**0.006**
	[0.001, 0.04]	[0.001, 0.293]	[0.001, 0.058]	[0.001, 0.060]

estimated through OLS and WLS regressions are generally identical. Compared with the estimates through WLS regression, the estimates by OLS regression show larger confidence intervals. However, for the cases in this article, the differences in confidence intervals did not affect the model determination. Meanwhile, the models through OLS regression are highly significant, with a large (greater than 0.99) regression coefficient

of determination. Overall, for all individual channels, the linear models through OLS regression depict the between-sensor relation well (see Fig. 13).

A cross-validation strategy was employed to demonstrate the associated improvements and model uncertainty. Cross-validation is a model validation technique, which has been widely used to assess how accurately a predictive model will perform on another data set. Similar to previous investigations [9], [10], the K-fold cross-validation ($K = 5$) with 10 000 simulations was performed for the transformation model (i.e., the transformation model of reflectance for the Landsat 3 MSS NIR1, see Fig. 14). Consequently, there were 50 000 validation cases totally for a transformation model. Specifically, for each validation case, 80% of samples were selected for training, and the rest 20% were for testing. Based on the training samples, the model coefficients were estimated through OLS regression, whereas the MRD of prediction (after
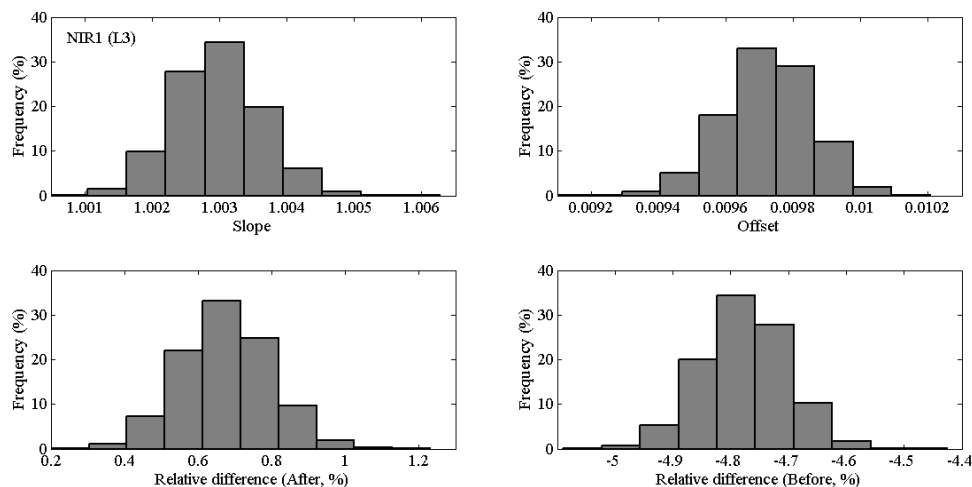
This article has been accepted for inclusion in a future issue of this journal. Content is final as presented, with the exception of pagination.

CHEN *et al.*: CHARACTERIZATION OF MSS CHANNEL REFLECTANCE AND DERIVED SPECTRAL INDICES
13

Fig. 14. Uncertainty and improvement associated with the linear transformation model for the Landsat 3 MSS NIR1 channel. (Top) Model coefficients ("Slope" and "Offset") are shown, while (Bottom) RDs (Left) after and (Right) before transformation are shown. The statistics in this figure were based on 10 000 times K-fold cross-validation ($K = 5$) tests.

TABLE V

COMPARISON OF THE LINEAR MODEL COEFFICIENTS FOR THE LANDSAT 3 MSS THROUGH OLS REGRESSION AND WLS. THE REGRESSION 95% CONFIDENCE INTERVALS FOR THE COEFFICIENT ESTIMATES ARE PROVIDED IN THE PARENTHESES, WITH LOWER CONFIDENCE BOUNDS AND UPPER CONFIDENCE BOUNDS, RESPECTIVELY

		Green	Red	NIR1	NIR2
Slope	OLS	**1.0178**	**1.0003**	**1.0030**	**0.9940**
		[1.0172, 1.0184]	[1.0001, 1.0003]	[1.0012, 1.0047]	[0.9934, 0.9947]
		1.0228[a]	*0.9879*	*1.0391*	*1.0058*
	WLS	**1.0179**	**1.0003**	1.0030	**0.9940**
		[1.0178, 1.0179]	[1.0003, 1.0003][b]	[1.0030, 1.0030]	[0.9940, 0.9940]
Offset	OLS	**0.087e-2**	**-0.270e-2**	**0.97e-2**	**0.37e-2**
		[0.079, 0.094]e-2	[-0.28, -0.27]e-2	[0.93, 1.01]e-2	[0.35, 0.39]e-2
	WLS	**0.087e-2**	**-0.27e-2**	**0.97e-2**	**0.37e-2**
		[0.087, 0.087]e-2	[-0.27, -0.27]e-2	[0.97, 0.97]e-2	[0.37, 0.37]e-2

[a]Coefficient in italic is estimated with setting the Offset to zero.
[b]Same values of at the low upper confidence were resulted from the minor coefficient variation, which was eliminated through round processing.

transformation) and the MRD before transformation were measured based on the testing samples. Fig. 14 summarizes the results for the NIR1 channel of the Landsat 3 MSS based on the K-fold cross-validation ($K = 5$) tests. The distribution of "Offset" is significantly different from zero, indicating that the linear model with an offset (nonzero constant term) is reasonable for cross-sensor transformation. In addition, tests based on simulation data showed that compared with the model without offset, the model with "Offset" performed better in reducing the between-sensor difference. For example, regarding the Landsat 3 MSS, the MRDs of the red channel and NIR1 channels are 1.749% and −0.956%, respectively, for the model without offset, while those are −0.092% and −0.664%, respectively, for the model with offset.

Generally, the cross-validation tests show consistency with the regression confidence intervals (see Table V). Median estimates (i.e., "Slope" and "Offset") extracted from all K-fold cross-validation cases (see Fig. 14) are close to those in Table V correspondingly. The between-sensor comparability is significantly improved, as the mean RD for the Landsat 3 MSS NIR1 channel decreases to about 0.70% (median) from the original difference about −4.75% (median), showing accordance with Fig. 9. Findings indicate that the linear model through OLS regression is generally applicable for cross-sensor transformation to improve the Landsat 1–5

MSS reflectance consistency, showing consistency with previous findings [7]–[10]. However, both the advantages and disadvantages of the linear transformation model should be recognized. On one hand, the linear model, serving as a simple and easily applicable way [7]–[10], provides a useful method to improve the between-sensor comparability on average. On the other hand, a global liner model achieves the optimal solution over all samples, while may not be the best one for subsets. Consequently, by using the linear transformation model, amplified differences are observed mainly for samples with low reflectance (see Figs. 7 and 8) when between-sensor comparability is improved on average. To overcome its shortages, more other applicable strategies should be investigated further. In addition, the statistical significance of the model's coefficient (e.g., "Offset") is determined in terms of the hypothesis test and cross-validation test. However, the physical meaning of the offset has not been interpreted currently.

D. Transformation to Improve Consistency in Spectral Indices of the Landsat MSS

The RD for individual channels largely contributes to the biases in vegetation indices. Accordingly, the increased RD over low reflectance for the NIR1 channel (see Fig. 10) along with the improved comparability of the red channel (see Fig. 9)
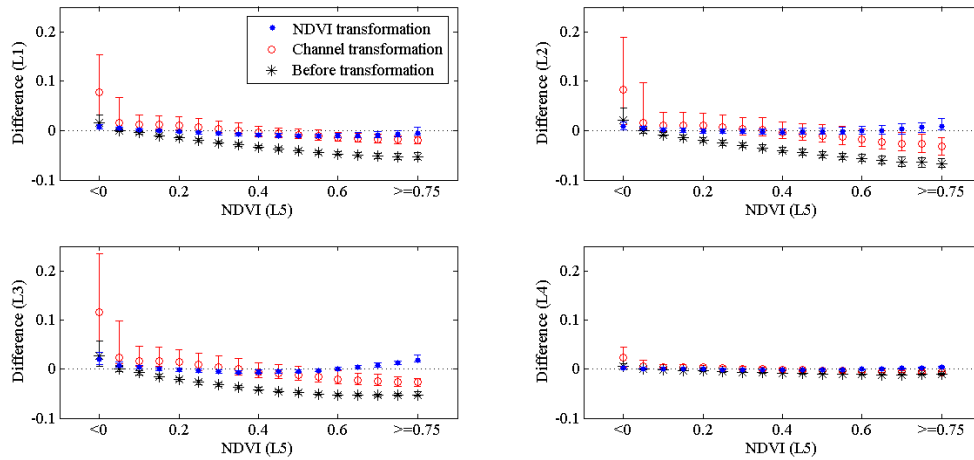
Fig. 15.   Between-sensor differences for NDVI of the Landsat 1-4 MSS, using the Landsat 5 MSS as reference. Two transformation strategies were performed separately, including the channel reflectance transformation (red) as an indirect strategy and the NDVI transformation (blue) as a direct strategy. The differences are shown by median (respective marks) and range (vertical lines) with the lower and upper taken as 5% and 95% percentiles, for contiguous 0.05 NDVI ranges of the Landsat 5 MSS.
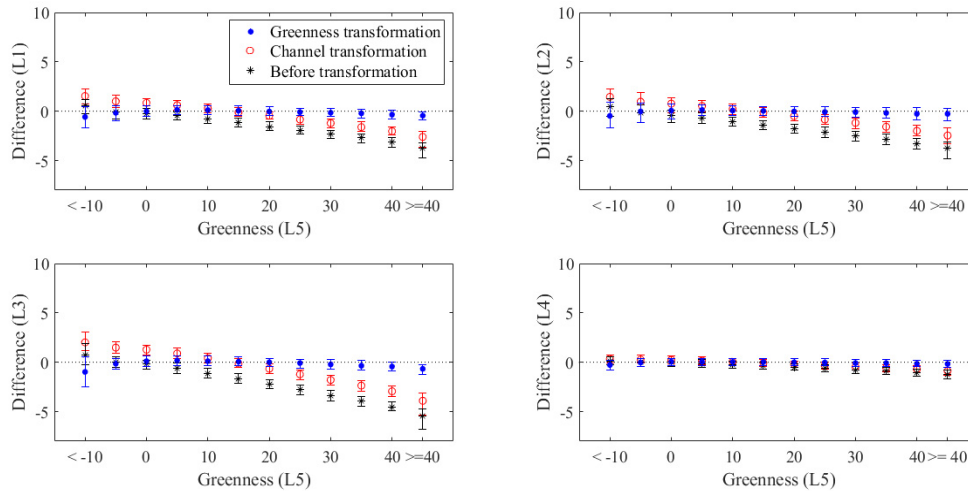

Fig. 16.   Between-sensor differences for the TC transformed greenness of the Landsat 1–4 MSS, using the Landsat 5 MSS as reference. Similar to Fig. 15, results separately based on two transformation strategies are presented. The differences are shown by median (respective marks) and range (vertical lines) with the lower and upper taken as 5% and 95% percentiles for contiguous five greenness ranges of the Landsat 5 MSS.

results in a visible difference in the vegetation indices followed by (see "Channel transformation" in Fig. 15). According to a previous investigation [56], two transformation strategies are possible for derived variables (i.e., vegetation indices), including retrieving the variable based on transformed channel reflectance correspondingly as an indirect strategy and getting the transformed variable using its specific model, respectively, as a direct strategy (see Figs. 15 and 16). Considering the amplified effects of individual channel differences, the vegetation indices should be transformed through their respective models directly (i.e., as "NDVI transformation" in Fig. 15) instead of recalculating the vegetation indices based on the transformed channel reflectance (as "channel transformation" in Fig. 15). Because of the direct transformation, the between-sensor inconsistencies of NDVI are significantly alleviated over all ranges. Meanwhile, there are obvious biases after the recalculation based on the transformed reflectance although the between-sensor comparability is generally improved. Actually,

we observed similar findings for the EVI2 (not shown) and the TC transformed greenness (see Fig. 16). To improve the between-sensor consistency of the derived variables from different MSS observations, it is more rational to transform the variables using their respective models directly.

E. Other Related Issues

Compared with the successive sensors (i.e., Landsat 4–5 TM, Landsat 7 ETM+, and Landsat 8 OLI), MSS has characterization shortages in design, such as in spatial resolution, spectral channels (i.e., number and spectral region), and radiometric resolution (see Table I). Significant omissions (undetection and underdetection) in cloud and cloud shadow are observable for the currently processed MSS archive in the Collection 1 Level-1 data product although reliable interpretation is largely possible for the region without cloud cover (see Fig. 17). The interpretation of QA band information is likely unreliable and affects autonomous analyses
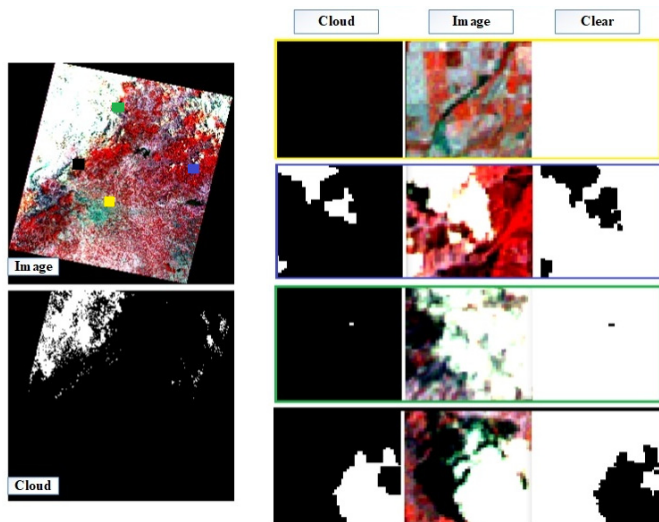
Fig. 17. Demonstration for the usability and uncertainty of the Landsat MSS QA band information in data quality interpretation at the pixel level: color image (R: NIR1 channel, G: green channel, and B; red channel). (Left) cloud mask of a full scene. (Right) cloud mask, color image, and clear terrain mask of four subsets covering different conditions (outlined with different colors correspondingly). Masks of cloud (with high confidence) and clear terrain were extracted according to the QA band information. The showcase is for a Landsat 4 MSS scene (LM04_L1TP_123032_19860307_20180331_01_T2) in the Collection 1 Level-1 data product, which was freely accessed at EarthExplorer (https://earthexplorer.usgs.gov/).

further, especially when time-series analyses at pixel-level are required [2]. Therefore, further improvements for the QA information of the MSS archive are required, such as in cloud detection [19]. Moreover, currently, the geo-registration accuracy of the MSS archive processed usually does not meet the Tier 1 requirements. For Landsat Collection 1 Level-1 data, scenes with the highest available data quality are placed into Tier 1 and are considered suitable for time-series analyses (https://www.usgs.gov/land-resources/nli/landsat/landsat-collection-1). From all the valid MSS scenes (totally 215 scenes) in Fig. 2, only one scene is assigned Tier 1. Taking into account impacts associated with the georegistration uncertainty, the averaged reflectance of a window with 7×7 pixels (locating within relative homogeneity) around each randomly selected sample was finally used in the comparison (see Fig. 11), as in [9].

The shortages in channel characterizations (i.e., spectral channels and radiometric resolution) may limit the MSS observations for the actual application, such as in land cover mapping, while findings varied among cases [20], [57], [58]. Nevertheless, from the MSS archive well processed, with the channels over the NIR region being sensitive to vegetation characteristics [28], the derived spectral features or indices (e.g., NDVI, EVI2, and the TC greenness as discussed in this article) are suggested valuable for time-series analyses. Further comparison and transformation to corresponding features from observations of other successive sensors (i.e., Landsat 4–5 TM, Landsat 7 ETM+, and Landsat 8 OLI) are required [9]. Major differences occur between the WRS-1 of Landsat 1–3 and the WRS-2 of the successive Landsats in repeat cycles, coverage, swathing patterns, and path/

row designators (https://landsat.gsfc.nasa.gov/the-worldwide-reference-system/). Therefore, associated issues challenging the Landsat consistency (both among the Landsat 1–5 MSS and between the MSS and its successors) are necessary to be tackled, whereas the spectral response function as the importance for sensor characterization was discussed comprehensively in this article.

VI. CONCLUSION

The characterization and comparison of the Landsat 1–5 MSS were comprehensively investigated in terms of derived spectral indices and the TC transformed features as well as channel reflectance. The investigations were mainly based on the synthesized reflectance obtained using a collection containing 10 000 Hyperion profiles of hyperspectral surface reflectance atmospherically corrected. The spectra profiles were collected over diverse geographical conditions, which suggests the investigation representativeness and the reliability of findings, as asserted previously [9], [17]. The Landsat 1–3 MSS show disagreement with the Landsat 5 MSS in channel reflectance, especially for the red channel (600–700 nm) (with median RDs varying from 2.3% to 6.3%) and the NIR1 channel (700–800 nm) (with median RDs varying from -1.8% to -4.8%). It results in significantly amplified biases with the median RD approximating 10%, for derived vegetation indices (i.e., NDVI and EVI2). Meanwhile, the Landsat 4 MSS was generally comparable to the Landsat 5 MSS. Findings suggested that the effect of the biases in individual channels was likely amplified on the normalized indices (as a nonlinear form) (i.e., NDVI and EVI2) through a complicated manner, while it was moderate or alleviated in the TC transformed features as a linear form.

To improve the comparability among the Landsat MSSs, in terms of reflectance and derived variables, the univariate linear transformation model through OLS regression was discussed accordingly. Confidence intervals of the coefficient estimates through OLS regression were overestimated due to data heteroscedasticity (see Table V). However, for the cases in this article, the overestimated confidence intervals did not affect the model determination, and unbiased OLS regression coefficient estimates were obtained. Overall, between-sensor comparability of channel reflectance was able to be improved through the OLS regression models, respectively. A small bias in individual channels may result in an obvious difference in the normalized vegetation indices, especially for low vegetation cases [10]. Consequently, to make the consistency for the vegetation indices (i.e., NDVI and EVI2) and the TC greenness, the direct strategy was more effective than using their respective transformation models compared with the indirect way by recalculating derived variables based on the transformed channel reflectance. The effectiveness of the transformation models was further demonstrated through case applications. However, both the advantages and shortages of the linear transformation model should be recognized, and more other applicable strategies should be investigated further.

Investigations in this article provided insights on the continuity issue of the Landsat MSS, which were mainly based

on the spectral response function served as an important characterization of the sensor [13], [33]. Findings on the Landsat 1–5 MSS may largely contribute to our knowledge on Landsat series especially for consistency issues, whereas most studies have focused on the successive sensors (e.g., TM, ETM+, and OLI) [6]. However, in practice, the consistency of derived variables from the Landsat MSS archive also relates to other factors, mainly including radiometric calibration [47], [59], georegistration [60], and atmospheric correction [7], [61], [62]. Resulted mainly from the shortages of sensor characterization, reliable detections of cloud and cloud shadow as well as atmospheric correction are difficult to MSS observations compared with other successive sensors. The georegistration problem of the MSS archive (i.e., mostly assigned Tier 2) challenges time-series analyses at pixel-level currently, which should be assessed further and to be improved properly. Considering the fact that the Landsat 1–5 MSS archive is continuing to be reprocessed (currently in the Landsat Collection 1 Level-1 data product), to take advantage of its historical importance in Earth observation, more investigations are necessary further. Furthermore, the Landsat 1–5 MSS have two channels over the NIR region although the NIR1 channel (700–800 nm) was used for vegetation indices in this article, whereas the successors (i.e., Landsat 4–5 TM, Landsat 7 ETM+, and Landsat 8 OLI) have one NIR channel. A proper interpolation method for vegetation index comparability between the Landsat 1–5 MSS and the successors is required. Therefore, more efforts are needed to evaluate the long-term consistency of the Landsat archive, including the MSS data, and to fully realize the benefit of the archive [2] although investigations in this article provide insights on continuity of the Landsat MSS data record. Finally, the importance of the continuity of reflectance and derived variables depends on specific applications.

REFERENCES

[1] T. R. Loveland and J. L. Dwyer, "Landsat: Building a strong future," *Remote Sens. Environ.*, vol. 122, pp. 22–29, Jul. 2012.

[2] M. A. Wulder *et al.*, "Current status of Landsat program, science, and applications," *Remote Sens. Environ.*, vol. 225, pp. 127–147, May 2019.

[3] C. E. Woodcock *et al.*, "Free access to Landsat imagery," *Science*, vol. 320, no. 5879, p. 1011, May 2008.

[4] M. A. Wulder *et al.*, "The global Landsat archive: Status, consolidation, and direction," *Remote Sens. Environ.*, vol. 185, pp. 271–283, Nov. 2016.

[5] Z. Zhu, "Change detection using Landsat time series: A review of frequencies, preprocessing, algorithms, and applications," *ISPRS J. Photogramm. Remote Sens.*, vol. 130, pp. 370–384, Aug. 2017.

[6] Z. Zhu *et al.*, "Benefits of the free and open Landsat data policy," *Remote Sens. Environ.*, vol. 224, pp. 382–385, Apr. 2019.

[7] D. P. Roy *et al.*, "Characterization of Landsat-7 to Landsat-8 reflective wavelength and normalized difference vegetation index continuity," *Remote Sens. Environ.*, vol. 185, pp. 57–70, Nov. 2016.

[8] P. Li, L. Jiang, and Z. Feng, "Cross-comparison of vegetation indices derived from Landsat-7 enhanced Tthematic mapper plus (ETM+) and Landsat-8 operational land imager (OLI) sensors," *Remote Sens.*, vol. 6, no. 1, pp. 310–329, Jan. 2014.

[9] F. Chen *et al.*, "Normalized difference vegetation index continuity of the Landsat 4-5 MSS and TM: Investigations based on simulation," *Remote Sens.*, vol. 11, no. 14, p. 1681, Jul. 2019.

[10] F. Chen, S. Lou, Q. Fan, J. Li, C. Wang, and M. Claverie, "A preliminary investigation on comparison and transformation of SENTINEL-2 MSI and Landsat 8 OLI," *ISPRS Arch.*, vol. 3, no. 3, pp. 2619–2624 Apr. 2018.

[11] P. S. Barry, J. Mendenhall, P. Jarecke, M. Folkman, J. Pearlman, and B. Markham, "EO-1 hyperion hyperspectral aggregation and comparison with EO-1 advanced land imager and landsat 7 ETM+," in *Proc. IEEE Int. Geosci. Remote Sens. Symp.*, vol. 3, Jun. 2002, pp. 1648–1651.

[12] K. G. Nikolakopoulos, P. I. Tsombos, G. A. Skianis, and D. A. Vaiopoulos, "EO-1 Hyperion and ALI bands simulation to Landsat 7 ETM+ bands for mineral mapping in Milos Island," in *Proc. SPIE, 8th Remote Sens. Environ. Monit., GIS Appl., Geol.*, Cardiff, U.K., vol. 7110, Sep. 2008, Art. no. 711010.

[13] G. Chander *et al.*, "Applications of spectral band adjustment factors (SBAF) for cross-calibration," *IEEE Trans. Geosci. Remote Sens.*, vol. 51, no. 3, pp. 1267–1281, Mar. 2013.

[14] Z. Wen, S. Zhang, S. Wu, F. Liu, and Y. Jiang, "Evaluating the consistency of multi-source wideband remote sensing images: A band simulation approach using Hyperion data," *J. Remote Sens.* , vol. 17, no. 6, pp. 1533–1545, Nov. 2013.

[15] C. T. Pinto, "Evaluation of the uncertainty in the spectral band adjustment factor (SBAF) for cross-calibration using Monte Carlo simulation," *Remote Sens. Lett.*, vol. 7, no. 9, pp. 837–846, Sep. 2016.

[16] M. Claverie, J. G. Masek, J. Ju, and J. L. Dungan. (2017). *Harmonized Landsat-8 Sentinel-2 (HLS) Product User's Guide*. Assessed: Jul. 3, 2018. [Online]. Available: https://hls.gsfc.nasa.gov/documents/

[17] M. Claverie *et al.*, "The harmonized landsat and Sentinel-2 surface reflectance data set," *Remote Sens. Environ.*, vol. 219, pp. 145–161, Dec. 2018.

[18] D. Pflugmacher, W. B. Cohen, and R. E. Kennedy, "Using Landsat-derived disturbance history (1972–2010) to predict current forest structure," *Remote Sens. Environ.*, vol. 122, pp. 146–165, Jul. 2012.

[19] J. D. Braaten, W. B. Cohen, and Z. Yang, "Automated cloud and cloud shadow identification in Landsat MSS imagery for temperate ecosystems," *Remote Sens. Environ.*, vol. 169, pp. 128–138, Nov. 2015.

[20] V. F. Renó, E. M. L. M. Novo, C. Suemitsu, C. D. Rennó, and T. S. F. Silva, "Assessment of deforestation in the lower Amazon floodplain using historical landsat MSS/TM imagery," *Remote Sens. Environ.*, vol. 115, no. 12, pp. 3446–3456, Dec. 2011.

[21] M. Vittek, A. Brink, F. Donnay, D. Simonetti, and B. Desclée, "Land cover change monitoring using Landsat MSS/TM satellite image data over West Africa between 1975 and 1990," *Remote Sens.*, vol. 6, no. 1, pp. 658–676, Jan. 2014.

[22] F. L. Lobo, M. P. F. Costa, and E. M. L. M. Novo, "Time-series analysis of Landsat-MSS/TM/OLI images over Amazonian waters impacted by gold mining activities," *Remote Sens. Environ.*, vol. 157, pp. 170–184, Feb. 2015.

[23] K. C. Fickas, W. B. Cohen, and Z. Yang, "Landsat-based monitoring of annual wetland change in the Willamette valley of Oregon, USA from 1972 to 2012," *Wetlands Ecol. Manage.*, vol. 24, no. 1, pp. 73–92, Feb. 2016.

[24] V. Markogianni and E. Dimitriou, "Landuse and NDVI change analysis of sperchios river basin (Greece) with different spatial resolution sensor data by Landsat/MSS/TM and OLI," *Desalination Water Treatment*, vol. 57, no. 60, pp. 29092–29103, Dec. 2016.

[25] S. Savage *et al.*, "Shifts in forest structure in Northwest Montana from 1972 to 2015 using the Landsat archive from multispectral scanner to operational land imager," *Forests*, vol. 9, no. 4, p. 157, Apr. 2018.

[26] T. He *et al.*, "Evaluating land surface albedo estimation from Landsat MSS, TM, ETM +, and OLI data based on the unified direct estimation approach," *Remote Sens. Environ.*, vol. 204, pp. 181–196, Jan. 2018.

[27] R. J. Kauth and G. S. Thomas, "The tasselled cap—A graphic description of the spectral-temporal development of agricultural crops as seen by Landsat," in *Proc. Symp. Mach. Process. Remotely Sensed Data*, Indiana, GL, USA, Jun. 1976, pp. 41–51.

This article has been accepted for inclusion in a future issue of this journal. Content is final as presented, with the exception of pagination.

CHEN *et al.*: CHARACTERIZATION OF MSS CHANNEL REFLECTANCE AND DERIVED SPECTRAL INDICES 17

[28] C. J. Tucker, "Red and photographic infrared linear combinations for monitoring vegetation," *Remote Sens. Environ.*, vol. 8, no. 2, pp. 127–150, May 1979.

[29] Z. Jiang, A. Huete, K. Didan, and T. Miura, "Development of a two-band enhanced vegetation index without a blue band," *Remote Sens. Environ.*, vol. 112, no. 10, pp. 3833–3845, Oct. 2008.

[30] USGS. *Landsat Surface Reflectance-Derived Spectral Indices, Version 3.6.* Assessed: May 2, 2018. [Online]. Available: https:// landsat.usgs.gov/sites/default/files/documents/si_product_guide.pdf

[31] J. C. Jiménez-Muñoz and J. A. Sobrino, "A generalized single-channel method for retrieving land surface temperature from remote sensing data," *J. Geophys. Res., Atmos.*, vol. 108, no. D22, p. 4688, Nov. 2003.

[32] H. Hu, F. Chen, and Q. Wang, "Estimating the effective wavelength of the thermal band for accurate brightness temperature retrieval: Methods and comparison," in *Proc. IEEE Int. Conf. Spatial Data Mining Geographical Knowl. Services*, Fuzhou, China, Jun. 2011, pp. 330–334.

[33] F. Chen, S. Yang, Z. Su, and K. Wang, "Effect of emissivity uncertainty on surface temperature retrieval over urban areas: Investigations based on spectral libraries," *ISPRS J. Photogramm. Remote Sens.*, vol. 114, pp. 53–65, Apr. 2016.

[34] C. J. Tucker *et al.*, "An extended AVHRR 8 km NDVI dataset compatible with MODIS and SPOT vegetation NDVI data," *Int. J. Remote Sens.*, vol. 26, no. 20, pp. 4485–4498, Oct. 2005.

[35] J. M. Peña-Barragán, M. K. Ngugi, R. E. Plant, and J. Six, "Object-based crop identification using multiple vegetation indices, textural features and crop phenology," *Remote Sens. Environ.*, vol. 115, no. 6, pp. 1301–1316, Jun. 2011.

[36] B. O'Connor, E. Dwyer, F. Cawkwell, and L. Eklundh, "Spatio-temporal patterns in vegetation start of season across the island of Ireland using the MERIS global vegetation index," *ISPRS J. Photogramm. Remote Sens.*, vol. 68, pp. 79–94, Mar. 2012.

[37] A. Mohammadi, J. F. Costelloe, and D. Ryu, "Application of time series of remotely sensed normalized difference water, vegetation and moisture indices in characterizing flood dynamics of large-scale arid zone floodplains," *Remote Sens. Environ.*, vol. 190, pp. 70–82, Mar. 2017.

[38] L. Ulsig *et al.*, "Detecting inter-annual variations in the phenology of evergreen conifers using long-term MODIS vegetation index time series," *Remote Sens.*, vol. 9, no. 1, p. 49, Jan. 2017.

[39] Y. Zhu *et al.*, "Exploring the potential of WorldView-2 red-edge band-based vegetation indices for estimation of mangrove leaf area index with machine learning algorithms," *Remote Sens.*, vol. 9, no. 10, p. 1060, Oct. 2017.

[40] A. Huete, K. Didan, T. Miura, E. P. Rodriguez, X. Gao, and L. G. Ferreira, "Overview of the radiometric and biophysical performance of the MODIS vegetation indices," *Remote Sens. Environ.*, vol. 83, nos. 1–2, pp. 195–213, Nov. 2002.

[41] E. P. Crist and R. C. Cicone, "A physically-based transformation of thematic mapper data—The TM tasseled cap," *IEEE Trans. Geosci. Remote Sens.*, vol. GE-22, no. 3, pp. 256–263, May 1984.

[42] S. Jin and S. A. Sader, "Comparison of time series tasseled cap wetness and the normalized difference moisture index in detecting forest disturbances," *Remote Sens. Environ.*, vol. 94, no. 3, pp. 364–372, Feb. 2005.

[43] P. D. Pickell, T. Hermosilla, R. J. Frazier, N. C. Coops, and M. A. Wulder, "Forest recovery trends derived from Landsat time series for North American boreal forests," *Int. J. Remote Sens.*, vol. 37, no. 1, pp. 138–149, Jan. 2016.

[44] B. T. Wilson, J. F. Knight, and R. E. McRoberts, "Harmonic regression of landsat time series for modeling attributes from national forest inventory data," *ISPRS J. Photogramm. Remote Sens.*, vol. 137, pp. 29–46, Mar. 2018.

[45] C. Huang, B. Wylie, L. Yang, C. Homer, and G. Zylstra, "Derivation of a tasselled cap transformation based on Landsat 7 at-satellite reflectance," *Int. J. Remote Sens.*, vol. 23, no. 8, pp. 1741–1748, Jan. 2002.

[46] M. H. A. Baig, L. Zhang, T. Shuai, and Q. Tong, "Derivation of a tasselled cap transformation based on Landsat 8 at-satellite reflectance," *Remote Sens. Lett.*, vol. 5, no. 5, pp. 423–431, May 2014.

[47] G. Chander, B. L. Markham, and D. L. Helder, "Summary of current radiometric calibration coefficients for Landsat MSS, TM, ETM+, and EO-1 ALI sensors," *Remote Sens. Environ.*, vol. 113, no. 5, pp. 893–903, May 2009.

[48] B. L. Markham and J. L. Barker, "Spectral characterization of the Landsat-4 MSS sensors," *Photogramm. Eng. Remote Sens.*, vol. 49, no. 6, pp. 811–833, Jan. 1983.

[49] S. G. Ungar, E. M. Middleton, L. Ong, and P. Campbell, "EO-1 Hyperion onboard performance over eight years: Hyperion calibration," in *Proc. 6th EARSeL Imaging Spectrosc. SIG Workshop*, Tel Aviv, Israel, Mar. 2009, pp. 1–6.

[50] J. Czapla-Myers, L. Ong, K. Thome, and J. McCorkel, "Validation of EO-1 Hyperion and Advanced Land Imager using the radiometric calibration test site at Railroad Valley, Nevada," *IEEE J. Sel. Topics Appl. Earth Observ. Remote Sens.*, vol. 9, no. 2, pp. 816–826, Feb. 2016.

[51] F. Chen, S. Yang, K. Yin, and P. Chan, "Challenges to quantitative applications of Landsat observations for the urban thermal environment," *J. Environ. Sci.*, vol. 59, pp. 80–88, Sep. 2017.

[52] C. M. Jarque and A. K. Bera, "Efficient tests for normality, homoscedasticity and serial independence of regression residuals," *Econ. Lett.*, vol. 6, no. 3, pp. 255–259, Dec. 1980.

[53] C. E. Holden and C. E. Woodcock, "An analysis of Landsat 7 and Landsat 8 underflight data and the implications for time series investigations," *Remote Sens. Environ.*, vol. 185, pp. 16–36, Nov. 2016.

[54] H. K. Zhang *et al.*, "Characterization of Sentinel-2A and Landsat-8 top of atmosphere, surface, and nadir BRDF adjusted reflectance and NDVI differences," *Remote Sens. Environ.*, vol. 215, pp. 482–494, Sep. 2018.

[55] X. She, L. Zhang, Y. Cen, T. Wu, C. Huang, and M. Baig, "Comparison of the continuity of vegetation indices derived from Landsat 8 OLI and Landsat 7 ETM+ data among different vegetation types," *Remote Sens.*, vol. 7, no. 10, pp. 13485–13506, 2015.

[56] F. Chen, L. Tang, C. Wang, and Q. Qiu, "Recovering of the thermal band of Landsat 7 SLC-off ETM+ image using CBERS as auxiliary data," *Adv. Space Res.*, vol. 48, no. 6, pp. 1086–1093, Sep. 2011.

[57] B. Haack, N. Bryant, and S. Adams, "An assessment of Landsat MSS and TM data for urban and near-urban land-cover digital classification," *Remote Sens. Environ.*, vol. 21, no. 2, pp. 201–213, Mar. 1987.

[58] M. Mohajane *et al.*, "Land Use/Land cover (LULC) using Landsat data series (MSS, TM, ETM+ and OLI) in Azrou forest, in the central middle atlas of Morocco," *Environments*, vol. 5, no. 12, p. 131, 2018.

[59] D. L. Helder, S. Karki, R. Bhatt, E. Micijevic, D. Aaron, and B. Jasinski, "Radiometric calibration of the Landsat MSS sensor series," *IEEE Trans. Geosci. Remote Sens.*, vol. 50, no. 6, pp. 2380–2399, Jun. 2012.

[60] G. Chander, D. L. Helder, D. Aaron, N. Mishra, and A. K. Shrestha, "Assessment of spectral, misregistration, and spatial uncertainties inherent in the cross-calibration study," *IEEE Trans. Geosci. Remote Sens.*, vol. 51, no. 3, pp. 1282–1296, Mar. 2013.

[61] M. Claverie, E. F. Vermote, B. Franch, and J. G. Masek, "Evaluation of the Landsat-5 TM and Landsat-7 ETM+ surface reflectance products," *Remote Sens. Environ.*, vol. 169, pp. 390–403, Nov. 2015.

[62] J. E. Vogelmann, A. L. Gallant, H. Shi, and Z. Zhu, "Perspectives on monitoring gradual change across the continuity of Landsat sensors using time-series data," *Remote Sens. Environ.*, vol. 185, pp. 258–270, Nov. 2016.
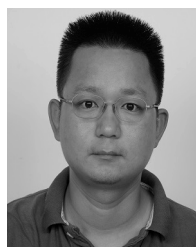
Feng Chen received the B.S. degree in geoinformatics from the China University of Petroleum, Beijing, China, in 2005, the M.S. degree in physical geography from the Institute of Geodesy and Geophysics, Chinese Academy of Sciences, Beijing, China, in 2008, and the Ph.D. degree in meteorology from Sun Yat-sen University, Guangzhou, China, in 2016.

He was a Research Scientist with the Institute of Urban Environment, Chinese Academy of Sciences, from 2008 to 2013. He has been with the Fujian Key Laboratory of Sensing and Computing for Smart Cities, Xiamen University, Xiamen, China, since 2016. He has been a Deputy Director with the Big Data Institute of Digital Natural Disaster Monitoring in Fujian, Xiamen University of Technology, since 2020. He has authored more than 30 articles. His research interests mainly include urban remote sensing, environment assessment and management, urban health, and sustainability.

Qiancong Fan received the B.S. degree from Southwest Jiaotong University, Chengdu, China, in 2016, and the M.S. degree from Xiamen University, Xiamen, China, in 2019.

His research interests include computer vision and remote sensing image processing, especially on object detection and SAR image processing.

Shenlong Lou received the B.S. degree in electronic information engineering from Zhejiang Agricultural and Forestry University, Zhejiang, China, in 2017. He is pursuing the M.S. degree in information and communication engineering with Xiamen University, Xiamen, China.

His major research fields are remote sensing image analysis and super-resolution reconstruction.

Limin Yang received the Ph.D. degree in geography from the University of Nebraska-Lincoln, Lincoln, NE, USA, with a specialization in climatology and remote sensing.

He has been involved in research on global and regional land cover characterization and land cover change monitoring via remote sensing since late 1980s. He has accumulated a wealth of experience in remote sensing, climatology, Earth system science, and global change research. He is a Visiting Professor with the College of Resources Environment and Tourism and Institute of Geoinformation Science and Technology, Capital Normal University, Beijing, China.

Chenxing Wang received the Ph.D. degree in environmental economic and environmental management from the Research Center for Eco-Environmental Sciences, Chinese Academy of Sciences, Beijing, China, in 2016.

She is focusing on urban sustainability toward human well-being.

Martin Claverie received the Ph.D. degree in environmental science from Paul Sabatier University, Toulouse, France, in 2012.

From 2013 to 2017, he was in charge of the implementation of the Harmonized Landsat Sentinel-2 (HLS) data set at the National Aeronautics and Space Administration (NASA), Goddard Space Flight Center, Greenbelt, MD, USA. He is with the Université Catholique de Louvain, ttignies-Louvain-la-Neuve, Belgium, where his research interest is focused on large scale crop yield forecasting using optical remote sensing.

Cheng Wang (Senior Member, IEEE) received the Ph.D. degree in signal and information processing from the National University of Defense Technology, Changsha, China, in 2002.

He is a Professor with the School of Informatics, and the Executive Director with the Fujian Key Laboratory of Sensing and Computing for Smart Cities, Xiamen University, Xiamen, China. He has coauthored more than 150 articles in refereed journals and top conferences. His research interests include point cloud analysis, multisensor fusion, mobile mapping, and geospatial big data.

Dr. Wang is a fellow of the Institution of Engineering and Technology, and the Chair of the Working Group I/6 on Multi-Sensor Integration and Fusion of the ISPRS. He was a recipient of the ISPRS Giuseppe Inghilleri Award for 2020.

José Marcato Junior (Member, IEEE) received the Ph.D. degree in cartographic science from the Sao Paulo State University, Sao Paulo, Brazil.

He is a Professor with the Faculty of Engineering, Architecture and Urbanism and Geography, Federal University of Mato Grosso do Sul, Campo Grande, Brazil. He has authored more than 30 in refereed journals and over 70 in conferences. His research interests include UAV photogrammetry and deep neural networks for object detection, classification, and segmentation.

Wesley Nunes Gonçalves (Member, IEEE) received the Ph.D. degree in computational physics from the University of Sao Paulo, Sao Paul, Brazil.

He is a Professor with the Faculty of Computer Science and Faculty of Engineering, Architecture and Urbanism and Geography, Federal University of Mato Grosso do Sul, Campo Grande, Brazil. He has authored more than 30 in refereed journals and over 60 in conferences. His research interests include computer vision, machine learning, deep neural networks for object detection, classification, and segmentation.

Jonathan Li (Senior Member, IEEE) received the Ph.D. degree in geomatics engineering from the University of Cape Town, Cape Town, South Africa, in 2000.

He is a Professor and the Head of the Mobile Sensing and Geodata Science Group, Department of Geography and Environmental Management, cross-appointed with the Department of Systems Design Engineering, University of Waterloo, Waterloo, ON, Canada. He is also a Founding Member of the Waterloo Artificial Intelligence Institute, Waterloo. He has coauthored more than 400 publications, over 200 of which were published in refereed journals, including IEEE-TGRS, IEEE-TITS, IEEE-JSTARS, IEEE-GRSL, *ISPRS-JPRS*, and *RSE*. His research interests include AI-based information extraction from LiDAR point clouds and earth observation images.

Dr. Li was a recipient of the Outstanding Achievement in Mobile Mapping Technology Award in 2019 and the ISPRS Samuel Gamble Award in 2020. He is the Chair of the ISPRS WG I/2 on LiDAR, Air- and Space-borne Optical Sensing from 2016 to 2021 and the ICA Commission on Sensor-driven Mapping from 2019 to 2023. He is an Associate Editor of the IEEE-TITS, the IEEE-JSTARS, and the *Canadian Journal of Remote Sensing*.